ASSESSMENT OF SOIL PROPERTIES USING MICROSCOPE BASED COMPUTER VISION

By

Bharath Sudarsan

Department of Bioresource Engineering

Faculty of Agricultural and Environmental Sciences

McGill University, Montreal

December 2015

A thesis submitted in partial fulfillment of the requirements of

the degree of Master of Science

ABSTRACT

Soil texture and organic matter content are important indicators of the quality and health of soil. They affect a range of soil properties and processes, which are fundamental for agriculture and civil engineering. Several traditional methods and advanced measurement techniques aim to address the challenge of quantifying these attributes. However, their cost, time requirements, sophisticated analytical methods and *in-situ* inapplicability pose a major challenge to rapid measurement. This research discloses the development of a new, inexpensive, microscope-based sensor system to estimate content of both sand and organic matter. The research was divided into two experiments conducted over a span of two years, each approaching the problem from two different computational perspectives. The first experiment involved images of air dried soil samples from Field 26 (acquired in 2014, organic soil) of the Macdonald Campus Farm of McGill University. The set of images was analyzed for sand and organic matter content using color and spatial image analysis, then validated against data obtained using conventional methods in a laboratory. Predictive relationships were developed using simple linear regressions based on parameters computed from the acquired imagery, such as hue, saturation, value, porosity, and variance estimates. The best sand and organic matter prediction models exhibited coefficients of determination (R^2) values of 0.63 and 0.83, respectively, with RMSE = 84.7 g/kg for sand content and 0.11 for log SOM. In addition to the first set of images, the second experiment explored both laboratory and *in situ* measurements from Field 86 (acquired in 2015, mineral soil). This method used a continuous wavelet transform to characterize sand content which was in strong agreement with the laboratory measurements (r^2 = 0.86 and RMSE = 44.7 g/kg for organic soil; r^2 = 0.87 and RMSE = 40.2 g/kg for mineral soil). However, the efficiency of this algorithm was subpar for the images collected *in-situ* (r^2 = 0.48 and RMSE = 80.6 g/kg).

This was due to the excessive soil water content, which can be addressed by modifying the microscope holder design and data collection protocol. The portable nature of the image acquisition system and the good performance of the wavelet algorithm shows promise for the future use of the system to rapidly quantify key soil physical attributes.

RÉSUMÉ

La texture du sol et la teneur en matière organique sont des indicateurs importants de la qualité et de la santé du sol. Ils affectent un grand nombre de propriétés et de procédés du sol, plus précisément ils sont essentiels dans les secteurs de l’agriculture et du génie civil. En considérant ces derniers attributs, plusieurs processus traditionnels et techniques de prises de mesures avancées ont pour but de les quantifier. Toutefois, leurs coûts, leurs temps, les méthodes d'analyse sophistiquées et inadaptable en pratique *in situ* posent un défi majeur à la mesure rapide. Cette recherche révèle la conception et le développement d’un système de traitement d’image qui prédit la texture du sol et la quantité de matière organique présente. Cette recherche a été conçue de deux manières différentes sur l’espace de deux ans. Les deux méthodes de résolution ont été faites à base des algorithmes. Pour le premier procédé, des images d’échantillons de sols séchés à l’air en provenance du terrain 26 de la ferme du campus Macdonald ont été utilisées (datant de l’année 2014, sol organique) . La base de données d’images a été analysée afin de reconnaître le contenu de sable et de matière organique du sol. Ceci a été possible en appliquant l’analyse des données géospatiales tout en validant avec les données obtenues par méthode conventionnelle en laboratoire. Des relations prédictives ont été développées par des simples régressions linéaires établies sur le contenu de sable et de matière organique du sol. Ceci a été possible en utilisant différents paramètres calculés de l'imagerie acquise tels que la teinte, la saturation, la valeur, la porosité et les estimés de variance. Les modèles de prédictions pour le contenu de sable et matière organique obtiennent des coefficients de déterminations (R^2) de 0.63 et 0.83. Tout cela avec une racine carrée du précédent (RMSE) de 84.7 g/kg pour le contenu de sable et 0.11 log sur le marché boursier. En addition de la première base de données d’images, la deuxième expérience a exploré à la fois les données prises en laboratoire ainsi que les mesures prises *in-situ* du terrain 86. (datant de l’année 2014, sol minéral) Ce procédé a utilisé la transformée en ondelettes continue pour caractérisé le contenu de sable. Cette méthode confirme avec les données du laboratoire (r^2 = - 0.86 et RMSE = - 44.7 g/kg pour le sol organique, r^2 = - 0.87 ; RMSE = - 40.2 g/kg pour le sol minéral). Cependant, l’efficacité de cet algorithme pour les images *in-situ* était bien moins précise (r^2 = – 0.48 ; et RMSE - 80.6 g/kg). Ceci était dû à la grande quantité d’eau présente dans le sol et pourrait être effectué avec des modifications au support pour le microscope et au protocol. La mobilité du système d'acquisition d'images et de la bonne performance de l'algorithme d’ondelettes sont prometteuses pour l’utilisation future du système développé pour quantifier rapidement les principaux attributs physique du sol.

.

ACKNOWLEDGEMENTS

First, I would like to sincerely recognize my parents' efforts for giving me this opportunity to pursue my postgraduate studies. I express my deepest gratitude to my mother and father for prioritizing my education above everything else through challenging times and for having faith in me.

Next I would like to thank Dr. Viacheslav Adamchuk. His patience and care was a great source of reassurance and guidance in the spheres of both academic research and my personal life. He was a mentor when I needed him for which I am deeply grateful.

I express my gratitude to Dr. Asim Biswas for his support and guidance with several of my research queries with his in-depth knowledge about soil and mathematical computation techniques. His insightful guidance, during the second half of my research, was invaluable.

I would like to mention my friend and colleague, Mr. Michael Saminsky, for being a peer and a pillar of support throughout my masters research tenure from the very beginning. From aiding in sampling the field to statistical analysis, his presence and inputs were crucial and welcome. I would like to thank him for a beautiful friendship and pleasant memories.

I thank all of the faculty and staff members in the department of Bioresource Engineering for providing a friendly atmosphere for research work. I offer my appreciation to Mrs. Hélène Lalande for her co-operation in the laboratory. My sincere gratitude also goes to all fellow members of the Precision Agriculture and Sensor Systems research team, especially Dr. Wenjun Ji, Dr. Nandkishor Dhawale and Mrs. Hsin-Hui Huang for their advice, support and insight which helped immensely with the project. I would also like to thank Ms. Karoline Deitrich and

Mr. Michael Saminsky for editing my thesis and Ms. Yasmeen Hitti for translating the abstract of the thesis into French.

Finally, I would like to thank the light of knowledge, the source of curiosity and ever pervasive wisdom which shines in all of us for this interesting journey of life I am on.

CONTRIBUTIONS OF AUTHORS

This research discussed in thesis has been submitted for publication in a peer reviewed journal. The author of this thesis was responsible for the development and evaluation of a computer vision based soil property sensor system. The author also designed and carried out the experimental and analytical work to meet the research objectives of this thesis. He is also responsible for the preparation of the manuscript based on this thesis. Dr. Viacheslav Adamchuk, an Associate Professor in the Department of Bioresource Engineering of McGill University, is the thesis supervisor. Dr. Adamchuk created the idea for this research and offered scientific advice and technical guidance throughout the study. Dr. Asim Biswas is an Assistant Professor in the Department of Natural Resource Sciences of McGill University; he constantly provided scientific suggestions for this study as a member of the author's graduate committee and helped with the development of the system with his insight on soil physics. Dr. Ji, a post-doctoral candidate in the Department of Bioresource Engineering of McGill University, provided valuable suggestions for analyzing the data with her detailed knowledge of statistics.

Publication related to the thesis

Sudarsan, B**.**, Ji, W., Biswas, A. and Adamchuk, V.I. Microscope-based computer vision to characterize soil texture and soil organic matter. *Biosystems Engineering* (under review).

Biswas, A., B. Sudarsan, W. Ji, and V. Adamchuk. 2015. Characterizing soil particle size distribution from images using continuous wavelet transforms. In: *Proceedings of the 4th Global Workshop on Proximal Soil Sensing*, Hangzhou, China, 12-15 May 2015, ed. Z. Shi, 90-95. Hangzhou, China: Zhejiang University.

Adamchuk, V., N. Dhawale, B. Sudarsan, J. Kaur, and A. Biswas. 2015. Automated on-the-spot analysis of physical, chemical and biological soil properties. In: *Proceedings of the 4th Global Workshop on Proximal Soil Sensing*, Hangzhou, China, 12-15 May 2015, ed. Z. Shi, 1-8. Hangzhou, China: Zhejiang University.

TABLE OF CONTENTS

LIST OF FIGURES

LIST OF TABLES

LIST OF ABBREVIATIONS AND SYMBOLS

B	Blue Plane of RGB color space
BLObs	Binary Large Objects
CCD	Charge Coupled Device
CMOS	Complementary Metal-Oxide Semiconductor
CWT	Continuous Wavelet Transform
DIP	Digital Image Processing
EC_a	Apparent Soil Electrical Conductivity
FAO	Food and Agriculture Organization
G	Green Plane of RGB color space
GWPS	Global Wavelet Power Spectrum
GWS	Global Wavelet Spectrum
H	Hue Plane of HSV color space
I1	2-µm sized moving windows on full image
I2	10-µm sized moving windows on full image
I3	50-µm sized moving windows on full image
I_e1	2-µm sized moving windows on eroded/masked image
I_e2	10-µm sized moving windows on eroded/masked image
I_e3	50-µm sized moving windows on eroded/masked image
NIR	Near-infrared
SOM	Soil Organic Matter
ROI	Regions of Interest
SSM	Site Specific Management

PSD	Particle Size Distribution
R	Red Plane of RGB color space
R^2	Coefficient of Determination
RMSE	Root Mean Square Error
S	Saturation Plane of HSV color space
V	Value Plane of HSV color space
USDA	United States Department of Agriculture

1 INTRODUCTION

Soil can be considered as the fundamental matrix of life and consequently, improper land use and poor management practices directly threaten the health of this matrix (Bezdicek et al., 1996). Knowledge of soil properties, like texture and organic matter content, can provide insight on soil health which, in turn, helps managers and other decision-makers improve soil conditions. Soil textural analysis is traditionally performed by sampling the soil and transporting it to a laboratory where a variety of techniques are performed in a sequence that begins with sieving and crushing, followed by measuring sedimentation using the hydrometer or pipette method (Smith & Mullins, 1991). Advanced technologies, such as laser diffraction and spectroscopic particle analysis techniques, can be used to estimate the texture of soil as well. The major constraint with the above mentioned methods is that they time consuming, labor intensive and expensive equipment. They are also restricted to laboratories and cannot be made compact for *in-situ* deployment.

Soil organic matter content was traditionally estimated in the laboratory using two techniques, namely, loss on ignition and Walkley-Black method of soil carbon content estimation (Nelson & Sommers, 1982). However, studies have shown that the loss on ignition technique does not completely account for all of the organic matter content in soil since not all organic matter ignites (Hoogsteen et al., 2015). Light reflectance has been correlated with organic matter content in soil by several studies (Krishnan et al., 1980). For many of the above mentioned techniques, samples need to be collected and transported to a laboratory where they would undergo standard preprocessing techniques, such as drying, crushing and sieving. These methods are laborious and the facilities required are expensive. Thus, there is a need to create a system that is efficient and cheap which could be deployed *in-situ* on the field to circumvent the expenses associated with sampling and transportation.

Computer vision technologies may be able to address this exact need as it requires only a camera and a computer for the process of measurement. The definition of digital image processing (DIP) according to R.M. Haralik and L.G. Shapiro is the science of creating, defining and testing an algorithm that is capable of automatically extracting and analyzing useful data from an image database. The data is analyzed by computational algorithms and the system does not require too many hardware components, thus, making it cheaper than techniques, such as spectroscopy and laser diffraction. Computer vision techniques have been used in several industries to study the particle size distributions (PSD). From sand particle size in mortars for cement and concrete (Mertens & Elsen, 2006) to froth parameters in ore extraction for the mining industry (Jahedsaravani et al., 2014), DIP based systems are applied in industry for commercial use. This wide range of usage illustrates the ability of such computational procedures to estimate the parameters of both large and particulate objects. However, there has not been comparable work on using computer vision techniques for soil particle analysis. This research study is focused on exploring the possibility of applying computer vision techniques for soil property analysis.

1.1 Research Objectives

The primary objective was to develop and evaluate a microscope image acquisition system suitable of *in-situ* use and to design a computational algorithm for analysis and prediction of soil properties (sand and organic matter contents). Two different computation methods were investigated. Method 1: assessment of soil texture using spatial statistics and SOM using a color-based prediction model. Method 2: quantification of sand content using wavelet analysis.

2 LITERATURE REVIEW

2.1 Importance of Soil Texture and Organic Matter

The soil matrix is an integral part of any ecosystem. Industrial agriculture over the past few decades has led to concerns over the excessive application of fertilizers and pesticides. The spatial variability of soil can lead to both under-application and over-application of chemicals in different parts of the same agricultural field (Anton et al., 2014). This led to the advent of Site-Specific Management (SSM), which involves a set of tools enabling the quantification of soil spatial variability - ultimately leading to improved and more precise agricultural management practices and more justified use of agricultural inputs.

Soil variability arises from varying physical properties and characteristics, which are predominantly determined by the percent composition of the three soil textural classes, namely, sand (2 mm - 0.05 mm), silt (0.05 mm - 0.002 mm) and clay (< 0.002 mm). Experimental research into the properties of soil texture can help farmers make informed management decisions (Barrios & Trejo, 2002). Soil texture analysis is one of the key components in studying many environmental issues. Studies by Yousefi et al. (2014) showed that plant available water content and least limiting water range measurements were highest under clay loam, thus, elucidating the effect of soil texture on these factors (Yousefi et al., 2014). Wind erosion of soil is also largely driven by soil textural properties (Nordstrom & Hotta, 2004). Research in China using simulated wind tunnels shows the range of the effects of wind erosion on different soil textures (Wang et al., 2006). Precision agriculture techniques aim to address the spatial variability of soils by changing the rate of application of chemicals at different locations based on field characteristics (Blackmer & White, 1998). Since most herbicide and pesticide recommendations are based on soil organic matter content, accurate quantification of soil organic matter is a necessity (Roberts et al., 2012).

2.2 Conventional Measuring Methods

Soil textural analysis is traditionally performed by sampling the soil and transporting it to a laboratory where a variety of techniques are performed in a sequence beginning with sieving and crushing, followed by measuring sedimentation using the hydrometer or pipette method (Smith & Mullins, 1991). These methods are costly, laborious, and time-consuming.

Recently, alternative laboratory analysis techniques have been developed to further improve accuracy and reduce analysis time by using advanced technologies. The laser diffraction method is one such method in which the particle size is established by determining the angle of diffraction by the particle under observation. Mie (Lorenz–Mie–Debye solution) theory quantifies the relationship between particle size and angular dispersion of light intensity (Keener et al., 2007). Other laboratory analysis methodologies, such as visible (vis) or near infra-red (NIR) spectroscopy, have been developed but they lack sufficient resolution. They can classify soil into light, medium, or heavy classes but the technique cannot provide any additional information about textural classes (Mouazen et al., 2007).

X-ray absorption is another example of a laboratory analysis technique. It is used to measure the density of the particles as they undergo sedimentation through a liquid medium (Stein, 1985). The size distribution of particle sizes is determined based on Stoke's law. The SediGraph® III 5120 (Micromeritics Instrument Corp., Atlanta, Georgia, USA) is a commercial system developed using micrometric and it is used to determine particles in the range of 0.1 μm to 300 μm.

Electrical sensing zone technology estimates the change in the value of the resistance across a small aperture as the soil particles pass through it. The system Elzone II 5390 (Micromeritics Instrument Corp., Atlanta, Georgia, USA) uses this technology; it is sensitive to particles in the range of 0.4 µm to 240 µm. The amplitude of the impedance values is proportional to the density of the particles passing through the aperture (Jackson et al., 1995). Technologies have also been designed to collect soil texture data in the field.

Traditional methods of measuring soil organic matter content are the loss on ignition and Walkley-Black method estimation (Nelson & Sommers, 1982). The Walkley-Black method uses potassium di-chromate, a strong oxidizing agent, to react with organic matter in the soil. This results in the conversion of chromium (VI) to chromium (III). The amount of organic matter corresponds to the amount of converted chromium which is measured spectrophotometrically. This assumes complete oxidation of all organic matter present, which may not be the case for all samples. On the other hand, the loss on ignition technique is a method where organic matter is ignited under controlled conditions and the organic matter content is estimated gravimetrically. Studies have shown that the loss on ignition technique might not represent soil organic matter completely as not all organic matter ignites (Hoogsteen et al., 2015).

Among the various factors that influence quantification of organic matter, optical reflectance plays a prominent role (Krishnan et al., 1980). Several studies have classified soil based on the correspondence of soil color against the Munsell color code (Schulze et al., 1993; Steinhardt & Franzmeier, 1979). Organic matter content is usually associated with high soil fertility and is observed as a dark surface horizon in the soil profile. Spectroscopic measurement of reflectance has proved to be more accurate at such color estimations than just visual inspection. Satellite imagery and aerial images provide a remote perspective to visualizing soil data. Brightness in these images is used in conjunction with elevation and electrical conductivity to delineate management zones within a field (Scharf et al., 2002; Schepers et al., 2004). However, studies that compared the efficiency of a ground based spectrometer with satellite imagery showed that the spectrometer was more accurate than the remote sensing data (Gomez et al., 2008).

NIR sensors have shown promise in predicting soil organic matter from an undisturbed soil core within a laboratory setting (Hummel et al., 2001). This research concluded by stating that further study was required to test the complete capabilities of the sensor (J. L. Shonk et al., 1991). Ground based sensors that use reflectance as a primary parameter to determine soil organic matter have shown some promise but they require site-specific calibration which is subject to several environmental characteristics, such as soil moisture, chemical composition of the soil, and parent material (Hummel et al., 2001).

The above measurement techniques share a few common characteristics. They are all indirect measurements of soil properties. The more accurate of these techniques are expensive, bulky, and are constrained to the confines of a laboratory setting. In contrast, methods based on image analysis utilize cameras to capture images of soil particles (dynamic or static images) and a simple computer code to categorize them. The size of the soil particles could be computed directly from the pixilated image using various computer vision algorithms following matching of textural patterns (Tuceryan & Jain, 1998). Soil organic matter content has been correlated with soil color (Steinhardt & Franzmeier, 1979). This data can extracted from a color images of soil.

2.3 Image Data Processing

A digital camera is a device that captures real life objects as images which are two dimensional matrices. These are digital signals sent to a frame grabber which is in turn connected to a computer that stores them as a digital matrix (Forsyth & Ponce, 2002). The digital image is then processed for features of interest. The definition of image processing according to Haralick and Shapiro (1992) is the science of creating, defining and testing an algorithm that is capable of automatically extracting and analyzing useful data from the image database. The basic steps of image processing are as follows:

- Image acquisition and storage.
- Image preprocessing.
- Image segmentation.
- Extraction of features of interest.
- Mathematical manipulation of interested data.

Computational procedures can be used to study the parameters of both large and particulate objects from a digital image. A study of the potential application of an image processing technique in the mining industry claims advantages, such as consistent results if the ambient light conditions are constant, continuous and non-invasive measurement, and low maintenance as there are no moving parts. (Crida & De Jager, 1997)

Just like any technology, image processing has some disadvantages. Low resolution of an inexpensive sensor is one such drawback. If the sensor is focused to a magnification level of a particle such as clay, then sand particles will be too large to be observed in the field of view. Another common issue includes the fact that image processing algorithms have the problem of occlusion. Since the image captured is in two dimensions, often an object in the field of view might result in another one hiding behind it.

2.3.1 Image Analysis in Similar Fields

Digital image processing (DIP) has been used extensively in the fields of defense and target acquisition. With the appropriate processor, it is possible to acquire and extract relevant information in real time. DIP is also used for pattern recognition analysis in fingerprint matching.

This technology utilizes detection of thickness of the ridge, orientation and direction of the ridge extending to various applications in criminology (Mardia et al., 1997). Intricate analysis applications of image processing extend into the domain of medical sciences. In this domain, the processing techniques are usually focused on enhancement of different scans, such as tomography, X-rays, and angiograms. The enhanced images are then scanned for detection of tumors or other objects of interest. The final step involves studying the geometries of the object detected (Pham et al., 2000). Research has been conducted in the use of image analysis tools to study the geometry of gravel particles up to 8 mm by performing object detection and elliptical fitting. This was used to extract the major and minor axis parameters for each gravel particle. The study by Strom et al. (2010) showed an automated grain sizing technique using DIP as an alternative to grid sampling and random pebble walk methods for river bed gravel sample analysis. In the field of metallurgy, image analysis techniques are used in the ore extraction stage and froth segmentation was useful for bubble size determination.

The above mentioned applications demonstrate the capability of image processing which might be extended to the study of characteristics of soil. In the next section, previous research that has attempted to apply computer vision techniques for estimating soil particle size distribution (PSD) is discussed.

2.3.2 Image Analysis in Soil PSD

Computer vision techniques are very efficient in detecting and matching textural patterns, which can be done directly in the field (Tuceryan & Jain, 1998). Studies have been conducted on soil profiles (White et al., 2005) and to predict susceptibility to landslides (Gökceoglu & Aksoy, 1996) using DIP. Fourier spectral analysis was used to process *in-situ* images of soil (Wilde et al., 2008); in this study, it was observed that partial description of the granular characteristics of soil is possible. Research by Shin and Hryciw (1996) states that there are two broad techniques for addressing the soil particle size distribution (PSD) – the deterministic and statistical methods. The former involves the use of object segmentation techniques such as edge detection and gray level thresholding, while the latter involves using a statistical approach for texture identification (Hryciw & Raschke, 1996). Deterministic methods of analysis produce considerable results only when the particles are not in contact with each other. This means that they must be spread on a surface with a source of illumination from behind the surface. The preprocessing techniques of the samples extend from crushing preparation of the sample to getting it ready for photography (Hryciw et al., 2006). Proper illumination conditions are essential for easy thresholding. This greatly limits the use of this technology to the confines of a laboratory.

Touching object separation or grain segmentation is a classic image processing problem. Watershed segmentation is suggested as a method for addressing this issue (Ghalib & Hryciw, 1999). It is observed that watershed segmentation usually produces a further complication, called over segmentation. This is addressed by a combination of several morphological operations to create markers for a marker based watershed segmentation technique. Geological research uses an image analysis technique for estimating the grain sizes from soft clastic sediments. However, the thin sections of geologic materials are placed on an optical enlarger and their imprints are collected on a photographic negative. The negative is then examined under a scanning electron microscope (Francus, 1998). Image analysis has also been used in the cement and concrete industry to categorize particle size distributions. However, in these studies, samples are impregnated with an epoxy resin to enhance the contrast of sand and to differentiate it from the pore space, which makes the detection of regions of interest computationally simple (Mertens & Elsen, 2006). Both of these methods require elaborate preprocessing that involves not just a camera but chemicals and negatives as prerequisites for the image analysis algorithms to be efficient.

An earlier attempt at using computer vision algorithms to characterize soil particle distribution is presented in Ghalib & Hryciw (1999). A CCD camera was used to capture images of soil samples placed on a platform and illuminated with light from underneath to make image segmentation easier. The use of a soil platform and back illumination techniques limit this method for *in-situ* data collection. Previous studies have shown that soil color classifications based on the Munsell color codes can be correlated with SOM (Schulze et al., 1993; Steinhardt & Franzmeier, 1979).

2.4 Wavelet Analysis

If the image is viewed as a data matrix, then a mathematical approach such as spectral analysis may be a powerful tool for tackling PSD problems. Wavelet analysis, in principle, divides the entire spatial series into different frequency components. Each of these components is analyzed using a scalable window, also referred to as the wavelet. The variations are computed by shifting the mother wavelet along the spatial series where it undergoes contractions and dilations. This results in a change in the length of intervals in time and space domain, thus, providing the information on scale.

When the space and time information is converted into scale information, the data becomes suitable available for computation. This has been applied in a variety of fields, such as seismic signal detection, atmospheric turbulence, image processing, optics, data compression, simulation, quantum mechanics, soil science, and geophysics (Biswas et al., 2008; Kumar & Foufoula-Georgiou, 1997). In an image matrix, an object can be identified as different from another by observing the pixels. There are variations in the image pixels in intensity plane or color planes between the two objects. Quantifying these variations at different scales will provide information on the variation in different particle sizes. Here, the continuous wavelet transform is used to characterize the scale specific variations which have the capability to describe the PSD of soil from images.

2.5 Summary

From the study of the literature, it is evident that though there are several efficient techniques for soil analysis, each has shortcomings. Feature extraction followed by advanced mathematical or computer vision techniques for studying and predicting various soil properties was deemed as an approach worth exploring. With recent advancements in technology, low-cost digital microscopes have become available on the market. For the purpose of this research, two unique methods have been developed and analyzed that address the specific problem of quantizing soil parameters from images under such a microscope in the laboratory and in field conditions.

3. MATERIALS AND METHODS

When a digital camera is pointed at an object, it focuses the reflected light with a focusing lens onto a digital sensor grid. This sensor grid is typically made of a charge coupled device (CCD) or a complementary metal-oxide semiconductor (CMOS) array. This is used to convert analog signals to digital data, thus, storing the object observed as an image matrix. This immediately suggests two methods to approach our problem.

The first approach is to consider the dataset as an image. This perspective would entail typical image processing steps such as preprocessing or noise removal, masking to highlight the objects of interest, then finally extracting relevant parameters for the prediction of soil properties. The second approach is to consider the dataset as an entire matrix of digital data. With this perspective, the entire matrix is considered and no special region is masked; instead, advanced mathematical techniques such as a wavelet are applied to decompose and directly analyze the entire matrix. Both of these methods were explored as two separate experiments.

3.1 Instrumentation and Hardware Design

A USB digital microscope AD 7013MT (Dino Lite, Inc., Taipei, Taiwan) was used to develop an image acquisition system in this study (Fig. 3.1). The microscope was chosen for its low cost, small size and large optical magnification (200X) at a 5 mega pixel resolution. The microscope was built in a durable aluminum alloy casing intended for outdoor usage (an important consideration for soil sensor development). A microscope holder was designed to provide a robust and sturdy framework for in field use in different weather conditions. The Teflon tube holder was designed with a press fitted scratch resistant fused silica viewing window of 40 mm diameter at the viewing end. The other end was sealed with a rubber stopper to prevent soil from entering the holder. The microscope was equipped with a ring of 7 LEDs for uniform illumination of the samples.

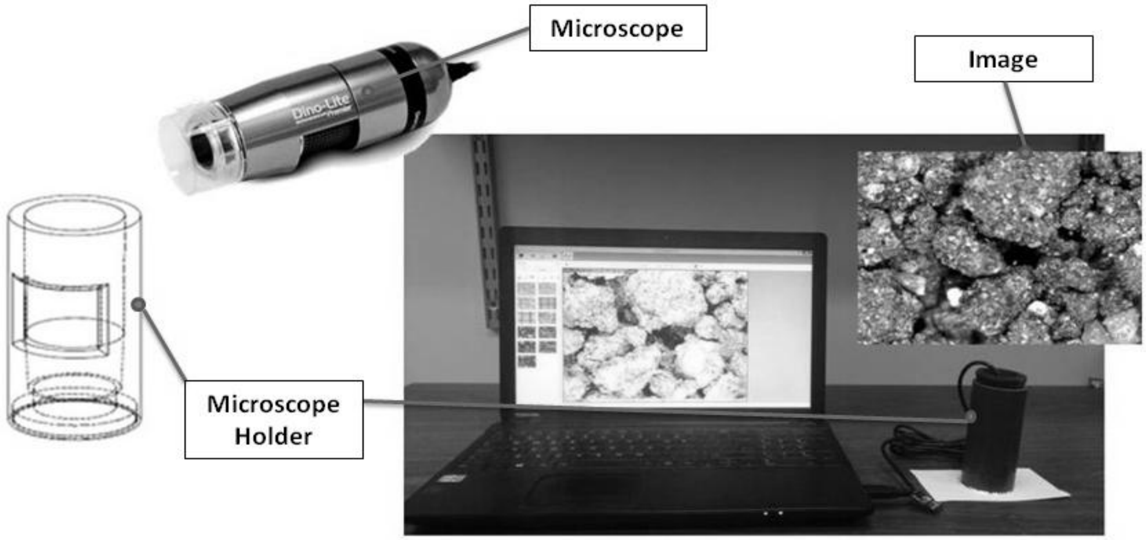

Fig. 3.1. The image acquisition system.

MATLAB (The MathWorks, Inc., Release:R2013a) software was used to control the image acquisition rate. The LED lights were also controlled using MATLAB. The intensity of the lights was set to 75% of its capacity to avoid overheating while maintaining adequate brightness for illuminating the samples. Studies with the Munsell color chart using Konica Minolta spectrophotometer CM-2600d (Konica Minolta, Inc., Tokyo, Japan) showed that controlled lighting conditions were necessary for estimating parameters based on color (Gómez-Robledo et al., 2013). Thus, the holder was designed to isolate the object under observation from any external light effects which tend to be unpredictable and weather-dependent.

3.2 Study 1

3.2.1 Site Description

For the first study in 2014, Field 26 (~11 ha) located on the Macdonald Campus Farm of McGill University, Ste-Anne-de-Bellevue, Quebec was chosen (45°25′N, 73°56′W). This field was chosen because it exhibited high spatial variability of soil texture ranging from sandy to clay loam soil. The soil series in Field 26 include: Muck, St. Zotique, Soulanges, Chicot, Upland, St. Damase, Farmington and Chateauguay series soils. Field 26 is also rich in organic matter as the covering muck soils are classified as organic materials according to the FAO definition of organic materials. The field was under corn-soybean rotation with the previous crop being corn in 2014 when soil was sampled.

3.2.2 Data Acquisition Protocol

3.2.2.1 Field Sampling Protocol

The soil sample collection was carried out in late April and early May 2014 before seeding. Here, 56 locations were selected following a stratified random sample design with nine additional locations representing field areas with diverse soil conditions. Sample locations were identified randomly within the 50 m × 50 m grid (quarter hectare). At each sampling location, surface residues were removed and the top soil (0 to 10 cm depth) samples were collected using a hand shovel. The samples were stored in air tight plastic bags and transported to the soil preprocessing station for image data. The maps in Fig. 3.2(a) and 3.2(b) illustrate these sampling locations on an elevation and EC map respectively. The elevation data in Fig. 3.2(a) was acquired using Trimble AgGPS 542 (Trimble Limited, Sunnyvale, California, USA) while the apparent soil electrical conductivity (EC_a) data in Fig. 3.2(b) was acquired using a DUALEM-21S (Dualem Inc. Milton, Ontario, Canada).

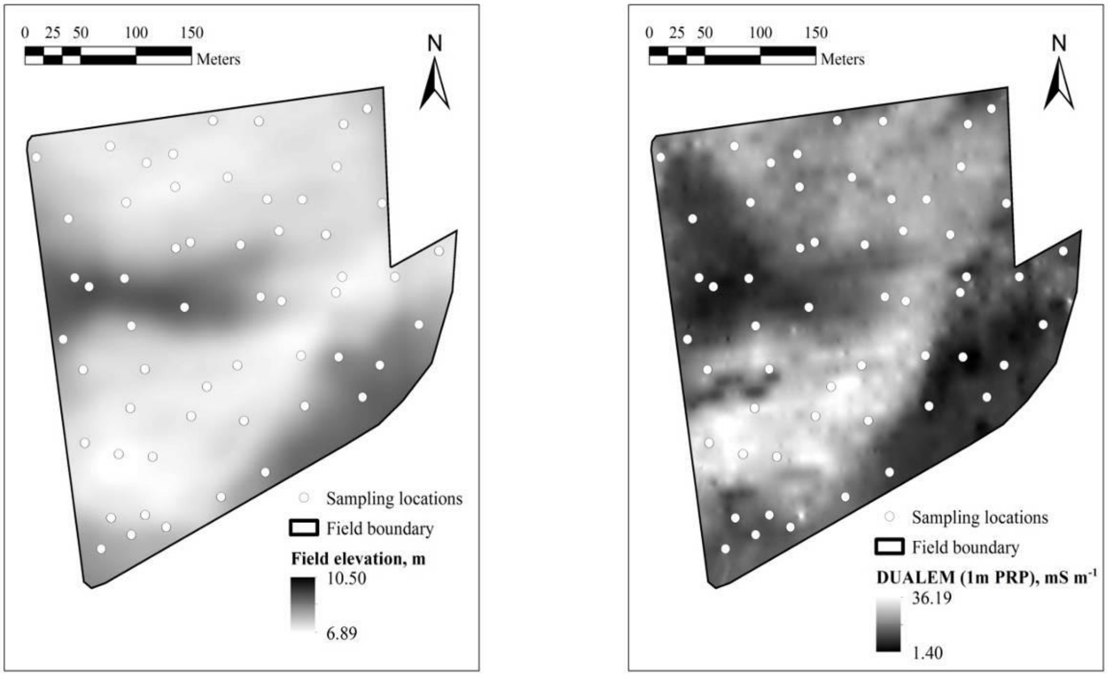

(a) (b)

Fig.3.2. Fifty six Sampling locations on a) elevation map and b) EC_a map of Field 26 of Macdonald Campus Farm, McGill University.

The soil samples are plotted on the USDA soil textural triangle (Fig. 3.3) to clearly illustrate the representativeness of the samples.

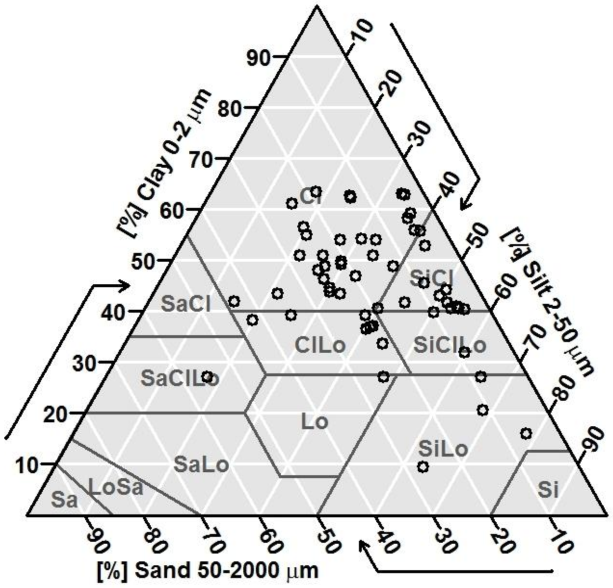

Fig. 3.3. Textural class of soil samples studied from Field 26.

3.2.2.2 Laboratory Analysis Method

The laboratory analysis was done in the Macdonald Campus Soil Laboratory. The soil samples were air dried, ground, and sieved through a 2 mm sieve. They were then stored in a labeled air tight container for image data collection followed by sedimentation and SOM analysis. After collecting microscope imagery data, fifty grams of each of the soil samples were weighed and transferred to a beaker. They were then treated with hydrogen peroxide on a hot water bath (Robinson, 1927). Once the effervescence subsided, the contents were transferred to a hydrometer for sedimentation analysis. Soil particle sizes were analyzed following the hydrometer method (Gee & Bouder, 1986). The contents of the hydrometer were transferred to be reweighed and placed on baking trays. These trays were placed in a soil oven at 105°C for 24 h. The loss of weight was used to compute SOM (Robinson, 1927).

3.2.3 Image Acquisition and Analysis

Images for each sample were collected by pressing the microscope holder on to the soil and controlling the camera directly from the computer. A set of three images were collected for each sample by mixing the soil sample to account for spatial variability. Thus, there were a total of 168 soil images taking into account three replicates for each of the 56 sample locations.

The image analysis was performed in two steps: masking and spatial analysis. Masking is an essential step in identifying the regions of interest which in our case are the particles on the aggregates. A well designed mask should be capable of segmenting the aggregates from the voids between them hence successfully separating the foreground, soil data from the background or void space data. The masking algorithm is composed of color scale transformation, preprocessing, thresholding, connected component analysis, and watershed analysis to create the mask.

3.2.3.1 Color Scale Transform

The RGB image was collected using the sensor and was transformed into grayscale.

$$\mathrm{f_g(x,y)} = 0.21\ \mathrm{f_R(x,y)} + 0.72\ \mathrm{f_G(x,y)} + 0.07\ \mathrm{f_B}(x,y) \tag{1}$$

where $f_g(x,y)$ is the grayscale value, $f_R(x,y)$ is the value of the pixel in the red plane, $f_G(x,y)$ is the value of the pixel in the green plane, and $f_B(x,y)$ is the value of the pixel in the blue plane. (Gonzalez et al., 2004).

3.2.3.2 Preprocessing

The soil aggregates (Fig. 3.4b) under the fused silica window can be disturbed by the smallest of perturbations that may originate from handling the holder. These micro-vibrations can cause blurred or distorted boundaries in the image. A standard image preprocessing technique was adopted to remove the distortions (Weiss, 2006). A burst of ten sub-images was taken with a sample interval of 10 ms and a median filter was applied to produce a single noise removed output image.

$$h_g(x,y) = med\{f_{g_i}(x-k, y-l)\}, (k, l \in W) \quad (2)$$

where $f_{g_i}(x,y)$ is the input gray images where i = 1:10; $h_g(x,y)$ was the output of the median filter; W was the two dimensional template.

Robust grayscale thresholding was a challenging process. Otsu (1975) global thresholding based on discriminate analysis theory was used to perform grayscale thresholding. Otsu's method assumes that the bimodal grayscale histogram originates from two Gaussian distributions of the foreground and background pixel values. For an ideal case, it would have been a clean segmentation. However, for microscopic soil images, the grayscale values of the coarse and fine textures were very similar. Hence, a simple Otsu thresholding will lead to inaccurate results and a bi-directional Otsu approach was implemented in this study. Using this approach, two windows W1 (1425 x 1425 pixels) and W2 (95 x 95 pixels) were chosen depending on the size of the possible objects of interest. This choice was made by analyzing a database of 168 images representing 56 sampling locations with three replications. It encompassed a range of aggregate sizes from 285 µm to 4275 µm. Thresholding was performed using the Otsu adaptive method (Otsu, 1975) on both window sizes (Figs. 3.4c and 3.4d).

Thus, for the gray image $h_g(x,y)$ with k gray levels, the probability class occurrence of ω_1 and ω_2 and probability distribution of p_i was

$$\omega_1 = \sum_{i=0}^{t} p_i \quad (3)$$

$$\omega_2 = \sum_{i=t+1}^{255} p_i \quad (4)$$

$$M_T = \frac{(\omega_1(t)M_1(t) + \omega_2(t)M_2(t))}{\omega_1(t) + \omega_2(t)} , \quad 0 \leq t < l \quad (5)$$

where M_T is the average gray level value in image $h_g(x, y)$; t is the gray level threshold; M_1 *and* M_2 are class means; $\omega_1(t)M_1(t)$ *and* $\omega 2(t)M_2(t)$ is the pixels in the image above and below the threshold *t*.

$$\sigma_B^2(t) = \frac{\omega_1(t)\omega_2(t)\left(M_1(t) - M_2(t)\right)^2}{\omega_1(t) + \omega_2(t)} \tag{6}$$

where $\sigma_B^2(t)$ is the variance between the two groups; *t* is the greatest $\sigma_B^2(t)$ is treated as the threshold *T* of an image *f (x, y).*

3.2.3.3 Minimum Threshold Matrix and Local Adaptive Binarization

For each pixel p of the image $h_g(x,y)$, two neighbourhood windows W1 and W2 were selected. The inspected pixel p was located at the centre of the windows where N_p^n and N_p^m denoted the bi-neighbourhood windows of pixel p with sizes of n x n and m x m, respectively. The n and m were odd integers. Thus, a local adaptive binarization mask was created. The minimum threshold among the two windows was chosen for each pixel. Let $T_{Otsu}\left(N_p^n, t\right)$ and $T_{Otsu}\left(N_p^m, t\right)$ denote the optimal thresholds of the two neighbourhoods.

$$f_b(x, y) = \begin{cases} 1 \text{ for } h_g(x, y) > min\left\{T_{Otsu}\left(N_p^n, t\right), T_{Otsu}\left(N_p^m, t\right)\right\} \\ 0 \quad \text{otherwise} \end{cases}, \text{ for each } p \in f. \tag{7}$$

where $f_b(x, y)$ is the binary image; $h_g(x, y)$ was the output of the median filter.

The remaining area in the mask was cleaned up by removing all Binary Large Objects (BLObs) less than 50 µm (Fig. 3.4e). A BLOb is a collection of binary data stored as a single entity within a database and it was identified as consistent image regions. It is a fundamental component of image analysis using machine vision. The BLObs were removed to avoid stray particles in the void spaces. The mask had connected objects in representing the soil aggregates as binary 1. The void space was set as binary 0. This led to the next challenge. All binary 1 regions or aggregate spaces were interconnected (Fig. 3.4f). Thus computationally, the algorithm would perceive the foreground of the binary image as a single, huge, inter-connected, aggregate particle. Hence, the particles were segmented.

3.2.3.4 Connected Component Labeling and Post-processing

Initially, the connected components were labeled to keep track of the number of objects in the binary image. Due to the porous nature of soil, tiny holes were identified within the aggregates. BLOb analysis was used to address this issue. A simple noise removal filter was applied to the labeled objects in the image. Any hole with smaller values than the noise threshold t_n was encountered in the binary image was flood filled.

$$\mathrm{f_b}(\mathrm{x,y}) = \begin{cases} 1 \text{ for } \mathrm{f_b}\ (\mathrm{x,y}) < tn \\ \mathrm{f_b}(\mathrm{x,y}) \text{ for } \mathrm{f_b}\ (\mathrm{x,y}) > tn \end{cases} \qquad t_n = 400 \tag{8}$$

where $f_b(x, y)$ is the binary image.

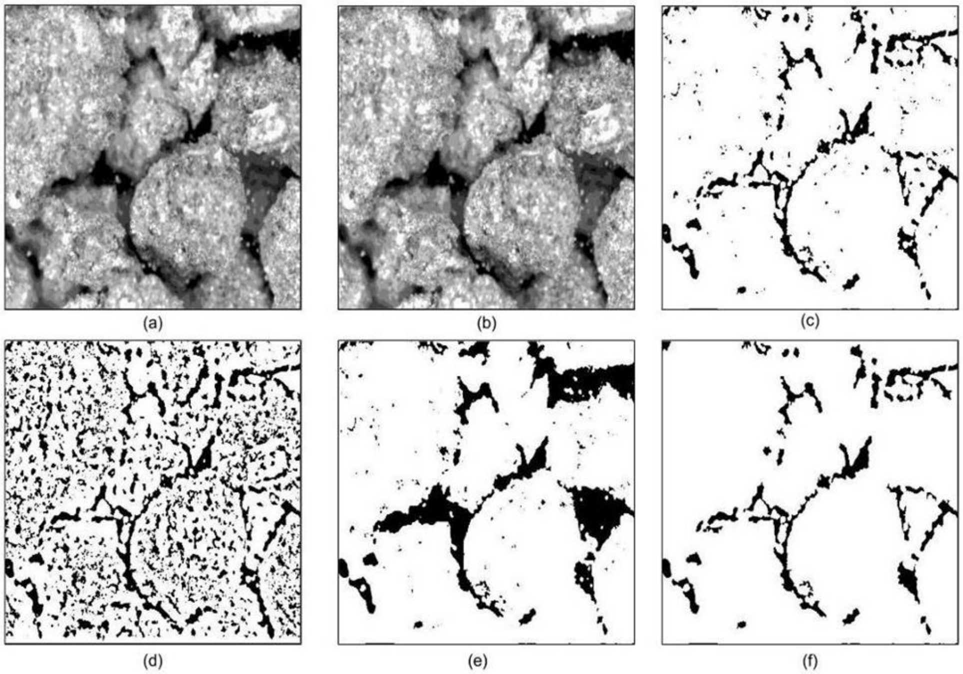

Fig. 3.4. First stage of mask generation; a) RGB color image; b) Grayscale image; c) Otsu local window 1; d) Otsu local window 2; e) Minimum threshold mask; and f) Post-processed mask.

3.2.3.5 Marker Detection

The output of the post-processing technique was used to perform the Euclidian distance transform to create an image skeleton (Fig. 3.5a) which was also known as the distance matrix (Maurer et al., 2003).

$$E_{Eucl} = \sqrt{(x_1 - x_2)^2 + (y_1 - y_2)^2} \tag{9}$$

where x_1, x_2, y_1 and y_2 are pixels from $f_b(x,y)$.

Extended minima were estimated for the skeletonised image (Fig. 3.5b) and imposed on the distance matrix (Soille, 1999) (Fig. 3.5c). As estimation of the markers improves the efficiency of the watershed segmentation algorithm (Moga & Gabbouj, 1998), markers were localized on a post-processed image in this study.

3.2.3.6 Watershed Segmentation

Watershed segmentation was a fast segmentation method. This algorithm was implemented to break the touching objects to successfully segment interconnected BLOBs into distinct labeled objects. However, small particles and noise tended to create over segmentation in this algorithm. This became even more challenging in dealing with particulate matter as objects of interest. This required a clear demarcation of the foreground from the background in the image. Marker based watershed segmentation was chosen to circumvent this problem. Skeletonization helped avoid over segmentation in the watershed segmentation process (Meyer, 1994) (Fig. 3.5d).

3.2.3.7 Morphological Operations

The mask was created and imposed on the gray image to highlight the regions of interest (foreground) or soil aggregates and to clearly distinguish them from the pores (background). In this study, the edges were made thicker to avoid edge effect. Small granules were avoided in the pore region between the aggregates. This was performed by eroding the segmented image using morphological erosion (Haralick et al., 1987).

$$A\theta B = \{Z | B_z \cup A^c \neq \phi \tag{10}$$

where erosion of A by B was the set of all structuring element z where the translated B has no overlap with the background of A (Gonzalez et al., 2004). The mask (Fig. 3.5 e) was then applied on the grayscale image. This enabled clear segmentation of void space from aggregates (Fig. 3.5 f).

$$\mathrm{f}\,(\mathrm{x},\mathrm{y}) = \begin{cases} \mathrm{f}\,(\mathrm{x},\mathrm{y}) \text{ for } \mathrm{f_b}(\mathrm{x},\mathrm{y}) = 1 \\ 0 \;\text{ for } \mathrm{f_b}(\mathrm{x},\mathrm{y}) = 0 \end{cases} \tag{11}$$

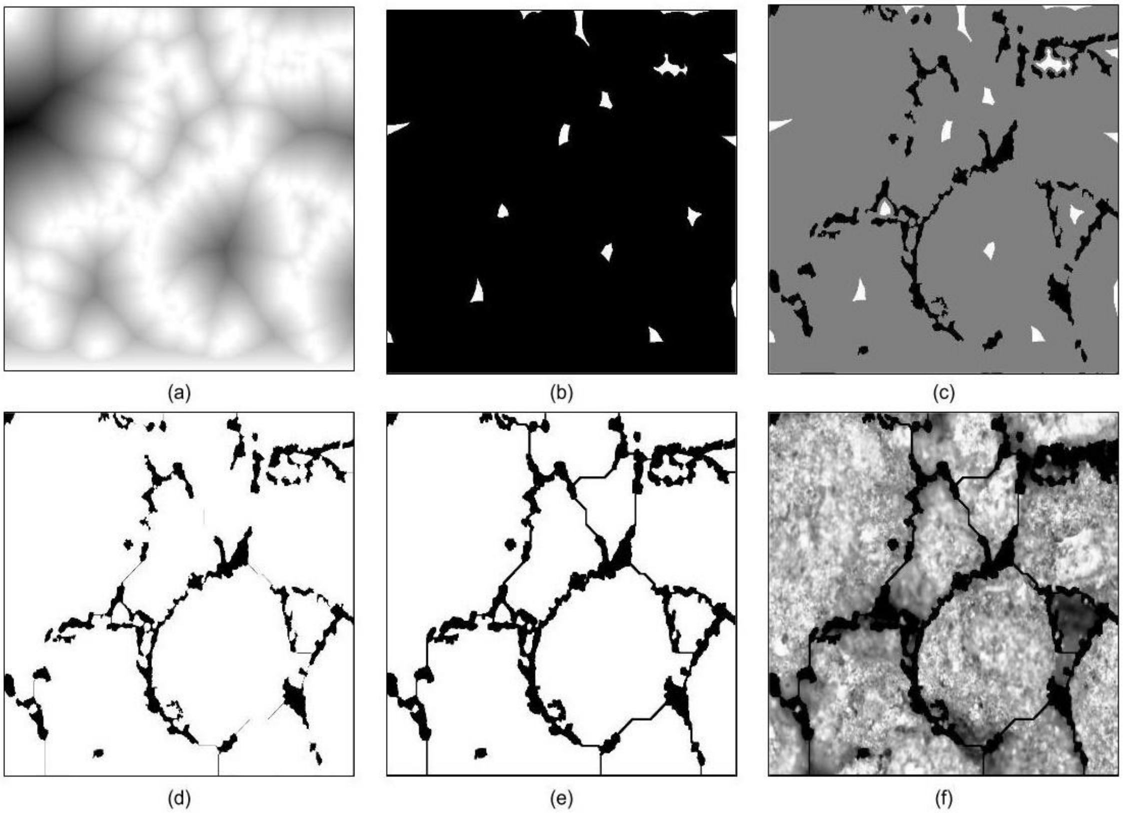

Fig. 3.5. Second stage of mask generation: a) Euclidian distance transform; b) detected minima; c) imposed minima; d) watershed segmentation; e) morphological edge enhancement; and f) gray image superposition (masking).

3.2.3.8 Spatial Computation

An 8 directional (3 × 3 pixel size with 8 pixels surrounding the centre pixel) moving window was created and applied to the image matrix. The variance between the center pixel and its neighbors was computed for each of the 8 directions. A temporary window was created with the variances in the location with the index corresponding to the respective neighbors. Once all the variances were computed and stored, the mean of these variances was assigned to the center pixel location. The window was then moved and the process was repeated. This resulted in a local variance matrix γ_p.

$$\gamma(\mathrm{x,y}) = 0.5\sqrt{F(x_p, y_p) - F(x\,,y)} \tag{12}$$

$$\gamma(\mathrm{x,y}) = \begin{cases} \mathrm{NaN\ for\ } \mathrm{f_b}(\mathrm{x,y}) = 0 \\ \gamma(\mathrm{x,y}) \mathrm{\ for\ } \mathrm{f_b}(\mathrm{x,y}) = 1 \end{cases} \tag{13}$$

$$\gamma_p = mean(\gamma(\mathrm{x,y})) \tag{14}$$

where $\gamma_{x,y}$ is the local variance of the pixels x, y in image *f(x,y)* and $F(x_p, y_p)$ is the center pixel. Note that the voids with zero values in this binary image are converted to NaN and the mean is computed for the NaN values. The two dimensional NaN mean is computed as the final step to give the moving window on intensity or 'I' parameter.

This technique was implemented for three different sizes of moving windows; 2µm (I1) - to define the silt-to-clay separation , 10 µm (I2) - to define the boundary between silt and fine sand and 50 µm (I3) - to describe the sand particles on both the masked images (I_e) and the raw full bitmap images (I). This generated a total of 6 parameters; the I_e1, I_e2, I_e3 and I1, I2, and I3. The RGB image was also transformed into the hue (H) saturation (S) and value (V) color space (Ford & Roberts, 1998). While RBG represented the Cartesian color coordinate system, the HSV represented a cylindrical color space equivalent of the former. The H indicated the degrees of color ranging from 0 to 360 where red was presented at 0 or 360. However, in the MATLAB calculation, the Hue (H) was represented with a scale range between 0 and 1, where 0 and 1 represented the red color, 0.33 represented the blue color and 0.66 represented the green color. Saturation (S) indicated the range of gray. A faded color was due to lower saturation levels, or in other words, the color contained more gray. MATLAB computes its saturation between 0 and 1, where 0 represented the color gray and 1 represented the primary color. Value was the brightness of the color and varied in conjunction with color saturation. An increase in the value resulted in an increase of color space brightness. MATLAB computations for value also ranged between 0 and 1, where the value ‘0’ indicated a complete dark version of a color (black) while 1 represented the brightest version of the same color. The average values of hue, saturation, and value were computed as H, S, and V parameters, respectively.

Porosity is defined as the ratio of volume of pores to total volume (Bear, 2013). The masking technique allowed for the computation of the void space area as the area of the regions in the binary image that have value zero.

$$A_p = \sum_{x=1}^{J}\sum_{y=1}^{K} \mathrm{f_b}(\mathrm{x,y}) \text{ for } \mathrm{f_b}(\mathrm{x,y}) = 0 \tag{15}$$

$$A_t = \sum_{x=1}^{J}\sum_{y=1}^{K} \mathrm{f_b}(\mathrm{x,y}) \tag{16}$$

$$Porosity = A_p/A_t \tag{17}$$

where $A_p$is the area of pores A_t was the total area. Porosity is a dimensionless unit.

3.2.3.9 Multivariate Stepwise Linear Regression

Predictive relationships between the image parameters (acquired from the processing of images) and the laboratory measured soil properties were developed using a multivariate stepwise linear regression. The parameters were found to be normally distributed based on examined skewness and kurtosis values and the Kolmogorov-Smirnov Z test. The collinearity between the parameters was examined using variance inflation factors and found to be absent. The normality in the distribution and absence of autocorrelation in the residuals were also examined and found to be suitable for developing the predictive relationship. The coefficient of determination (R^2) and the root mean square error (RMSE) were calculated to examine the performance of the relationship between laboratory measurements and microscope imagery-based predictions.

3.3 Study 2

3.3.1 Site Description

For study 2 in 2015, two agricultural fields were selected. Field 26 (~11 ha) and Field 86 (~17 ha) are located at the Macdonald Campus Farm of McGill University, Ste-Anne-de-Bellevue, Quebec, Canada (45°24′N, 73°56′W). Both fields exhibited high spatial variability in soil types ranging from organic to sandy soil and texture varying from sand to clay loam. The inter-field variability was also significant. Field 26 descriptions are given in section 3.2.1. Field 86 was sampled in 2015 for its rich mineral soils. It had soils from several series, including Chicot, Dalhousie, St-Bernard, Macdonald, St-Amable, Ste-Rosalie and Courval series. Both fields were under minimum-tillage practices and under a corn-soybean rotation with the previous crop being soybean in Field 26 and corn in Field 86 in 2014.

3.3.2 Data Acquisition Protocol

3.3.2.1 Field Sampling Protocol

In each of the locations, after the surface materials were scraped off (0-10 centimeters), an *in-situ* image was also collected using the microscope housed in the holder described in section 3.1. Following the image collection, physical soil samples were collected. The field boundaries and the location of the subsurface drainage system (tile drain system) were taken into consideration. The sample collection was carried out in late April and early May, 2015, before seeding. The soil samples were stored in two sets of air-tight plastic bags. One set was analyzed by Ward Laboratories Inc. in Kearney, Nebraska, USA. The other set was sent to the preprocessing station to be prepared for laboratory image acquisition.

For this study three sets of data were created. Table 3.1 provides a description of these datasets.

Table 3.1. Description of Datasets.

Dataset Number	Description	Number of Soil Samples	Sampling Season
Dataset 1 Organic Soil	Field 26 images acquired in lab from soil samples	56	Summer-2014
Dataset 2 Mineral Soil	Field 86 images acquired in lab from soil samples	67	Summer-2015
Dataset 3 Mineral Soil	Field 86 images acquired under *in-situ* conditions	67	Summer-2015

The soil samples were plotted on the USDA soil textural triangle (Fig. 3.6) to clearly illustrate the representativeness of the samples.

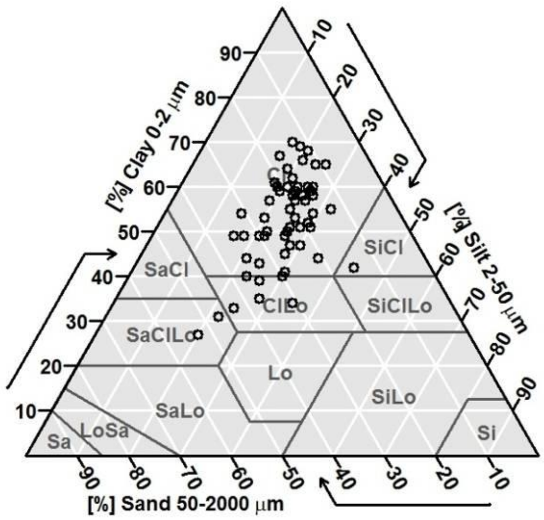

Fig. 3.6. Textural class of soil samples studied from Field 86.

The maps in Fig. 3.7(a) and 3.7(b) illustrate the sampling locations of Field 86 on an elevation and EC_a map respectively. The elevation data in Fig. 3.7(a) the apparent soil electrical conductivity data in Fig. 3.7(b) was acquired.

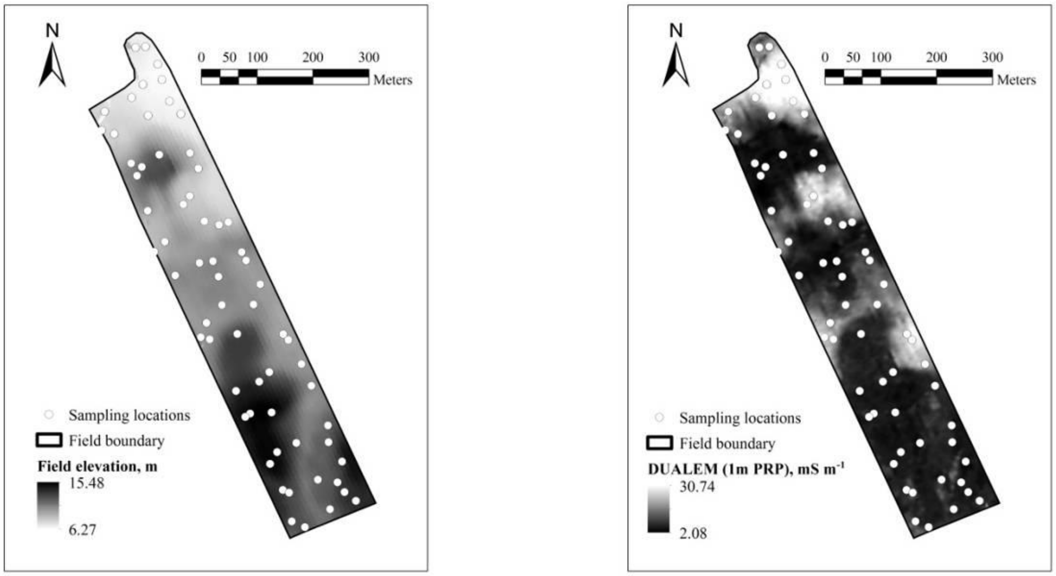

(a) (b)

Fig. 3.7. Sixty four sampling locations map on a) elevation map and b) EC_a map of Field 86 of Macdonald Campus Farm, McGill University.

3.3.2.2 Laboratory Analysis Technique

The soil samples analyzed at Ward Laboratories Inc. in Kearney, Nebraska, USA were analyzed using weight loss on ignition (LOI) for SOM estimation (Nelson & Sommers, 1982) and the hydrometer method for soil texture estimation. The results were sent via electronic mail.

3.3.3 Image Acquisition

For this study, three image sets were prepared (Table 3.1). Dataset 1 consisted of 168 (56 x 3 replicates) *ex-situ* soil images from Study 1 on Field 26 (2014), carried over for wavelet analysis. Dataset 2 consisted of 201 (67 x 3 replicates) *ex-situ* images of soil samples from Field 86. Dataset three consisted of 201 (67 x 3 replicates) *in-situ* images from Field 86.

3.3.4 Wavelet Analysis and Image Analysis

Wavelet analysis uses a mathematical function that occurs over finite spatial and temporal domains, also known as a wavelet, to study multi-scale processes. Wavelet results in a small and finite waveform unlike the Fourier series which extends indefinitely (Graps, 1995). The integral wavelet transform (e.g., the basic wavelet) and the wavelet series are the two main components of wavelet analysis. The wavelet series is expressed in terms of a single function by means of two operations, namely, binary dilations and integral transformations (Chui, 1992). Given a spatial series y_i measured at locations x_i (where i = 1, 2, 3 ... m) along a straight line, a mathematically integral wavelet transform can be defined as follows:

$$\mathrm{W}(\mathrm{s},\tau) = \int_{-\infty}^{\infty} y\,(x)\bar{\psi}_{s,\tau}\,(x)\,\mathrm{d}x \tag{18}$$

$$\text{where,}\qquad \bar{\psi}_{s,\tau}\,(x) = \frac{1}{\sqrt{\mathrm{s}}}\left(\frac{\mathrm{x}-\tau}{\mathrm{s}}\right) \tag{19}$$

where, $\psi(x)$ is the basic wavelet function and $\bar{\psi}_{s,\tau}$ is its complex conjugate. The parameter s is the dilation-contraction factor, and τ is the temporal or spatial translation of the wavelet function (Si, 2008).

In this study we implement only CWT. DWT's scales are analyzed in octaves (integer powers of 2) instead of voices (fractional powers of two), as it is done using CWT. Octave sampling may not always lead to a physically meaningful analysis of scale (Lau & Weng, 1995). Wavelet scale information is directly related to the size of the object under observation which in this instance is sand particle sizes and hence CWT was chosen over DWT. The detailed theory on CWT could be found at Chui (1992) and Mallet (1998). Briefly, given a spatial series Y_i of length N (where i

= 1, 2, 3 ... *n*), mathematically continuous wavelet transform coefficient $\mathrm{W_i^Y}$ can be calculated as follows:

$$\mathrm{W_i^Y(s)} = \sqrt{\frac{\mathrm{d}x}{\mathrm{s}}} \sum_{\mathrm{j=1}}^{\mathrm{N}} Y_j \psi \left[(\mathrm{j} - \mathrm{i}) \frac{\mathrm{d}x}{\mathrm{s}} \right] \tag{20}$$

where, *dx* is the equal sampling interval, *s* is the scaled wavelet, *x* is the translated wavelet, and ψ is the wavelet function (Torrence & Compo, 1998).

Commonly used wavelet functions in CWT include the Haar wavelet, Mexican hat and the Morlet wavelet. The Haar wavelet is asymmetric in nature and is used to detect sharp changes in the data series while the Mexican hat is real and symmetric in nature and is used to detect the peaks and valleys in the data series. The Morlet wavelet is complex symmetric and the imaginary part is used to extract phase information (Biswas & Si, 2011). Morlet wavelet was used in this study because of its ability to display much better resolution in spatial and frequency domains. The wavelet function $\psi(\eta)$ of the Morlet wavelet was defined as follows.

$$\psi(\eta) = \pi^{-1/4} e^{\mathrm{i}\varpi\eta - 0.5\eta^2} \tag{21}$$

where, η is the dimensionless space and ϖ is the dimensionless frequency.

The Morlet wavelet's imaginary part can also be used to extract the dominant orientation and variations in a random field. The energy associated with the scale and location can be measured from the magnitude of the Morlet wavelet. While calculating the wavelet coefficients, it was noted that it was biased towards the larger scales (Liu et al., 2007; Torrence & Compo, 1998). Liu et al. (2007) proposed a method used here to rectify this bias. This gives rise to a wavelet power spectrum measurement as it provides some idea about the interaction between space-frequency-energy in the spatial data series. For this study, the global wavelet power spectrum (GWPS) was computed. It was the average of the local wavelet spectra over all the location points (N). It was mathematically represented by:

$$\overline{W^{Y}}(s) = \frac{1}{N}\sum_{n=0}^{N-1}|W_{n}^{Y}(s)|^{2} \tag{22}$$

The Global wavelet transform (GWT) results in the global wavelet spectrum (GWS) which in turn provides a consistent estimation of the true power spectrum which was useful for the estimation of non-stationary data series. Spectral components are defined as frequency and period components are ordered according to period scales in GWS (Partal & Küçük, 2006). Therefore, the objective of this experimental study was to use CWT to characterize PSD from the images taken with a portable microscope in the laboratory setting.

The images are first transformed into grayscale and then analyzed using the CWT followed by GWT. To reduce the computational load, 20 evenly spaced rows (Dimension 1) and 20 evenly spaced columns (Dimension 2) are selected as a subset to represent the entire image matrix. For each row of data, the CWT spectra and GWT spectra were calculated. The GWT spectra are divided into two groups: “coarse” representing sand percentage (particles 2.0 mm to 0.05 mm) and “fine” representing the sum of silt and clay percentages (particles 0.05 mm and below). The fine and coarse fractions are computed for each of the 20 data series along both rows and columns. The average of the 20 rows and the average of the twenty columns were computed to give a single data series along each dimension, one representing the row average and another representing the column average. The mean of the corresponding row and column averages gives the final coarse and fine values which are compared against the laboratory measured data.

4 RESULTS AND DISCUSSION

4.1 Study 1

The descriptive statistics of soil properties are documented in Table 4.1. The sand values varied between 34.3 g/kg to 593 g/kg with an average of 328 g/kg and standard deviation of 146 g/kg. This elucidates that there was a wide range of distribution of sand within the study area. A similarly wide distribution was observed of SOM ranging from 54.7 g/kg to 728 g/kg with an average of 297 g/kg and standard deviation of 193 g/kg.

Table 4.1. Descriptive statistics of soil properties from Field 26 in 2014.

Parameters	Mean (g/kg)	STD (g/kg)	Min (g/kg)	Max (g/kg)
Sand	328	146	34.3	593
Silt	253	100	65.2	528
Clay	122	83.4	19.7	375
OM	297	193	54.7	728

Based on Field 26 data obtained in 2014, the descriptive statistics of various image parameters are presented in Table 4.2. The H values or the color range (for 168 images) varied between 0.12 and 0.23 with an average of 0.15 and a standard deviation of 0.015. This indicated that the majority of the image colors fall within the yellow range. The V values, or the brightness, ranged from 0.24 to 0.64 with an average of 0.45 and a standard deviation of 0.11. This indicated that the majority of the images fall within the lower half of the brightness range or they are darker in color. A smaller value of porosity indicated a low pore to the total area ratio. The porosity values ranged between 0.003 and 0.33 with an average of 0.10 and a standard deviation of 0.06. This indicates that on average, 10% of the image area was covered by pore spaces.

While the I_e3 values ranged from 0.90 to 4.43 with an average of 2.18 and a standard deviation of 0.18, the I_e2 values ranged from 0.46 to 2.95 with an average of 1.22 and a standard deviation of 0.50. This indicated that the average variance of the moving window size of 50 µm of the masked images was larger than the variance of the moving window size of 10 µm of the same image. A similar trend was observed between the window size of 50 µm and 1 µm of the masked image as the variance of the 1 µm and 10 µm window size were very similar. There was no obvious trend of increasing/decreasing variance with window size of either the masked or full image.

Table 4.2. Descriptive statistics of various image parameters.

Parameters	Mean	STD	Min	Max
H	0.15	0.02	0.12	0.24
S	0.20	0.03	0.12	0.27
V	0.45	0.11	0.24	0.64
Porosity	0.10	0.06	0.00	0.33
I_e3	2.18	0.78	0.90	4.43
$I3$	2.25	0.59	1.32	3.81
I_e1	1.41	0.15	1.24	2.05
$I1$	1.26	0.02	1.23	1.33
I_e2	1.22	0.50	0.46	2.95
$I2$	1.03	0.02	0.59	1.91

There has to be a fine balance between the number of parameters chosen and the predictive capability of the developed relationship as too many. Too few parameters can cause over simplification of the model (Noori et al., 2010). The overall dataset was into a training (60%) and validation (40%) dataset. Thus, the predictive model was trained with 33 soil samples randomly selected out of 56. Since there are three replicates in each sample, a total of 99 images were chosen with their parameters for the training dataset.

A step-wise mixed model analysis was adopted for developing the predictive relationship. The p-value threshold was set to 0.25 between the upper and lower limits. The overall dataset was grouped into three different sets of parameters and the predictive relationships were developed for each group of parameters. In group one, only raw image parameters were chosen; H, S, V, I1, I2 and I3. The relationship showed a coefficient of determination, $R^2 = 0.79$. In group two, only eroded image parameters were chosen; H, S, V, porosity, I_e1, I_e2 and I_e3. The $R^2 = 0.81$. Group three where all the parameters were chosen: H, S, V, porosity I_e1, I_e2, I_e3, I1, I2 and I3 resulted in $R^2 = 0.80$.

As there was no significant difference between R^2 values, eroded image parameters were chosen for further analysis. This choice was made for two main reasons; first, it makes more physical sense to compute variance among the regions of the image that represented the aggregates and not include the void space and secondly, the computation time was decreased for every image as the moving window did not compute variances for the NaN values.

The predictive relationship was expressed as:

$$Sand\ \left(\frac{g}{kg}\right) = 443 + 1504 \cdot H - 637 \cdot S + 1347 \cdot V - 410 \cdot Porosity + 269 \cdot I_e3 - 376 \cdot I_e2 \tag{23}$$

$$Log\ (organic\ matter) = 4.22 - 1.66 \cdot H - 3.29 \cdot V - 0.25 \cdot I_e3 + 0.331 \cdot I_e2 \tag{24}$$

The predictive relationship for sand can be adequately explained by the parameters in the equation. The inter-correlated Value (V) and Saturation (S) plane were directed towards the brightness of the image. This might be due to the fact that sand crystals in aggregates appeared brighter under the exposure of the LED lights of the microscope. The I2 and I3 window sizes were chosen as 10 μm and 50 μm. I3 was selected to represent the coarse to fine particle boundary (equivalent to sand and silt) while the I2 was chosen to depict the boundary between the fine and very fine particles. Thus, they also contributed positively to predicting the sand content of the images. The predictive relationship between the logarithm (base 10) of organic matter and the image parameters included H and V (not S). This may be due to the fact that the soils collected for this study had a very high amount of organic matter (min = 54.7 g/kg, max = 728 g/kg, and average = 297 g/kg) and were predominantly dark in color. Hence, the color and brightness corresponding to H and V parameters played a significant role in the prediction while the saturation (S) did not. Similar to the sand prediction, I2 and I3, the silt and sand boundary windows also played a significant role in predicting SOM. The parameter representing the smallest window size I1 was removed as it had high variance. The RMSE observed for the training models were 0.08 for SOM and 66.0 for sand g/kg. The training dataset was illustrated below in Fig. 4.1(a) and Fig. 4.1(b) for logarithm of organic matter and sand content respectively.

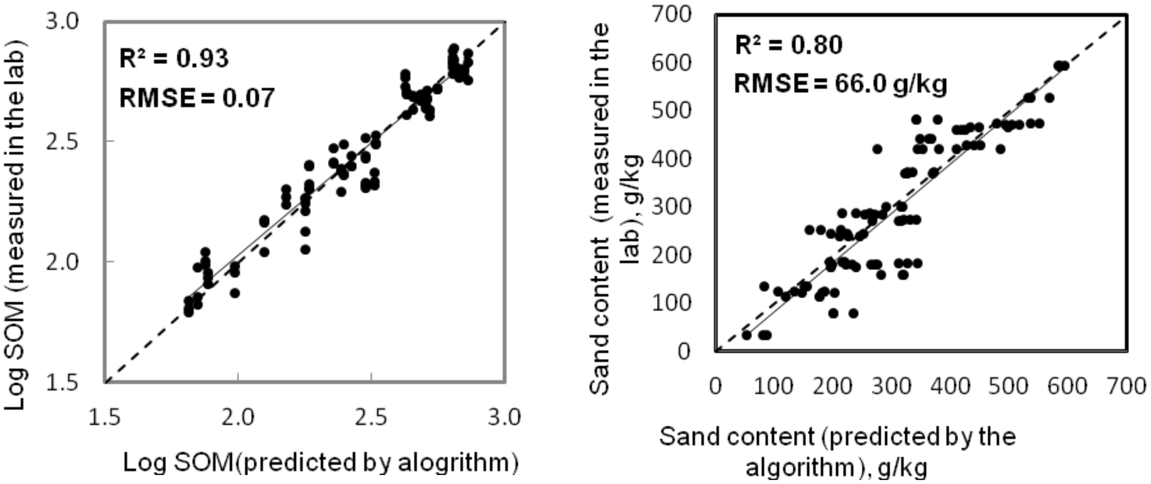

(a) (b)

Fig. 4.1. a) Training set model of the log of organic matter and b) The training set model of sand

content.

The relationship developed using the training data was applied to the testing dataset (remaining 40% of the data). The R^2 values on the testing dataset for SOM and sand content were 0.83 and 0.63, respectively. The RMSE values observed for them were 0.11 and 84.7 for organic matter and sand, respectively. This is shown below in Fig. 4.2(a) and Fig. 4.2(b) for logarithm of organic matter and sand content respectively.

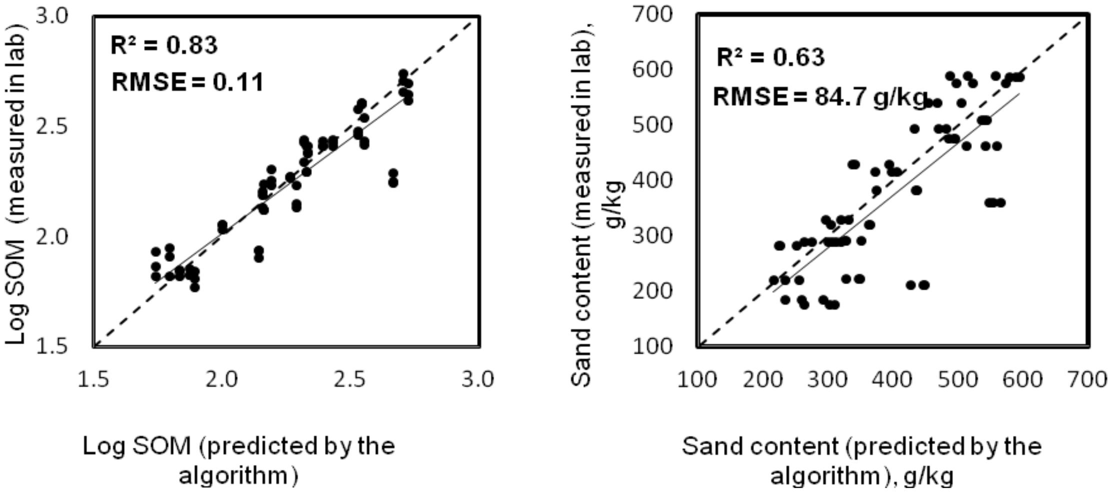

(a) (b)

Fig. 4.2. a) Testing set model of log of organic matter and b) The testing set model of sand content.

4.2 Method 2

The script written in MATLAB provides a visual representation of calculated GWPS in Fig. 4.3. Here is an example of an image of sample 40, replicate 01, from dataset 1, to illustrate how the data were interpreted.

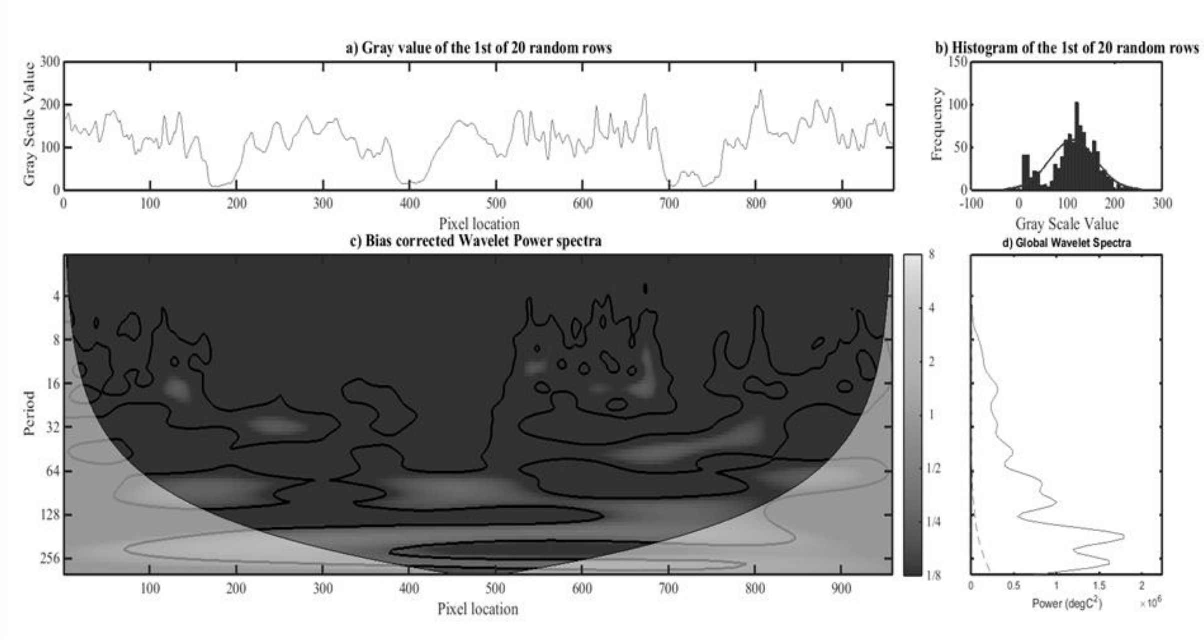

Fig. 4.3. a) Spatial distribution; b) histogram; c) wavelet spectrum; and d) global wavelet spectrum of the grayscale values selected from an image collected from Field 26 in 2014. The color scale shows the intensity of variations, thick solid line indicates 95% significance of those variations, and fine solid line indicates the cone of influence.

The bias corrected wavelet spectra show variations at different scales and locations while global wavelet spectra show the location normalized variations at different scales. The variations over scales are further separated into two groups, fine fractions and coarse fractions. Significant variations at a finer scale indicates higher amounts of clay and silt (47%) while stronger variations at a larger scale indicates higher amounts of sand (53%). The laboratory measured sand content for this sample was 54% and clay was 46%.

The dataset was not split into training and testing models and no calibration was requires, as particle size was directly predicted from the wavelet transform.

4.2.1 Dataset 1

Based on Field 26 laboratory images collected in 2014, the relationship between the laboratory measured and predicted (from image) fine fractions show a strong agreement (slope = 1.13, r^2 = 0.86, RMSE = 44.7 g/kg). (Fig.4.5). However, the deviation of the trend line in from the 1:1 line was statistically significant. This might be due to the fact that Field 26 was muck soil; thus, it has very high organic matter content. Organic matter tends to bind and hold soil together, forming micro-aggregates (Fig.4.4). The algorithm might misinterpret these micro aggregates as sand particles, causing the deviation of the trend line. The regression relationship shows the prediction capability of 86.9% for coarse fractions for the data. To test the robustness of the algorithm and for further validation, the script was run on an entirely different dataset collected from another field: Field 86. The samples were prepared using identical protocols and the results are discussed as follows.

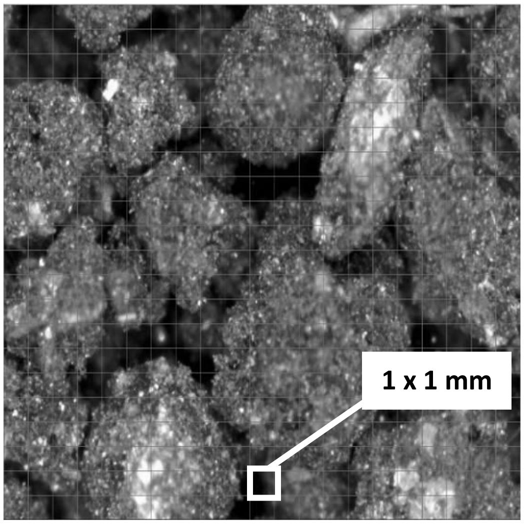

Fig. 4.4. Illustration of micro aggregates of soil sample 40 from Field 26.

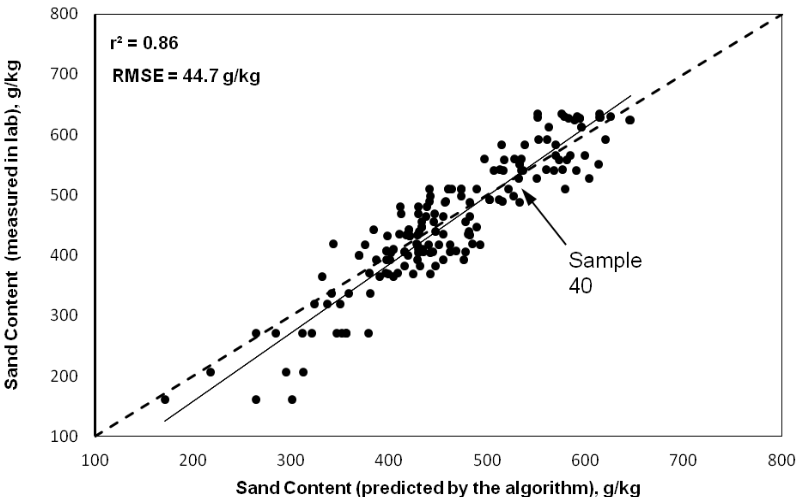

Fig. 4.5. Predicted particle sizes from images versus laboratory-measured particle sizes of Coarse fraction for dataset 1.

4.2.2 Dataset 2

The descriptive statistics for Field 86 are elaborated in table 4.3. The sand content varied from 27% to 70% with an average of 52.2%, while silt content varied from 15% to 43% with an average of 24%. The clay content varied greatly among the samples. The minimum, maximum, and average clay contents were 9%, 53% and 23.1%, respectively.

Table 4.3. Descriptive statistics of soil properties from Field 86 in 2015.

Parameters	Mean (g/kg)	STD (g/kg)	Min (g/kg)	Max (g/kg)
Sand	522	102	270	700
Silt	245	524	150	430
Clay	231	897	90	530

The relationship between the laboratory-measured values and predicted coarse fractions (Fig.4.6) shows strong agreement (slope = 0.92, r^2 = 0.87, RMSE = 40.2 g/kg). The deviation of the trend line from the 1:1 line was not statistically significant. This was because unlike Field 26, Field 86 shows more of a mineral soil nature. This may explain the smaller deviation unlike in dataset 1. The estimated error of sand content 40 g/kg is encouraging with regards to the implementation of this method for *in-situ* measurements.

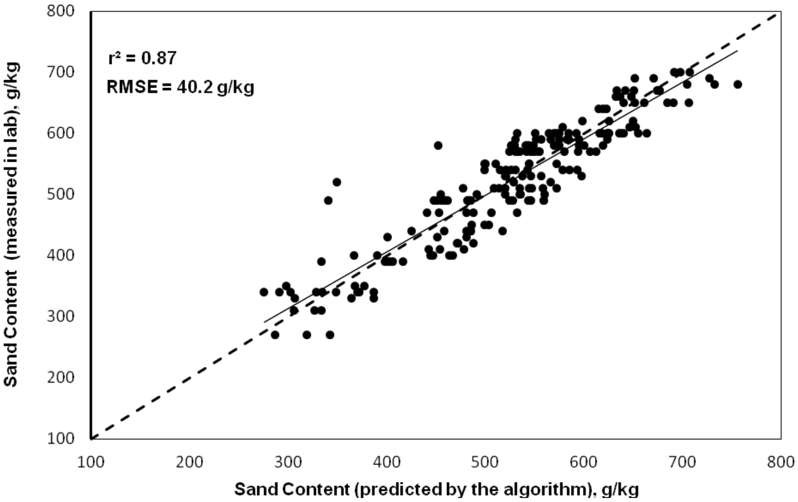

Fig. 4.6. Predicted particle sizes from images versus laboratory-measured particle sizes of coarse fraction for dataset 2.

4.2.3 Dataset 3

The relationships between the laboratory measured and the predicted fine fractions and coarse fractions are shown in Fig. 4.7. The deviation of the trend line from the 1:1 line was statistically significant (slope = 0.67, r^2 = 0.48, RMSE = 80.6 g/kg). Interestingly, this was a consequence of the image quality for this dataset. The images were poorer quality (as compared to the ones from the laboratory) due to issues associated with collecting data in field conditions.

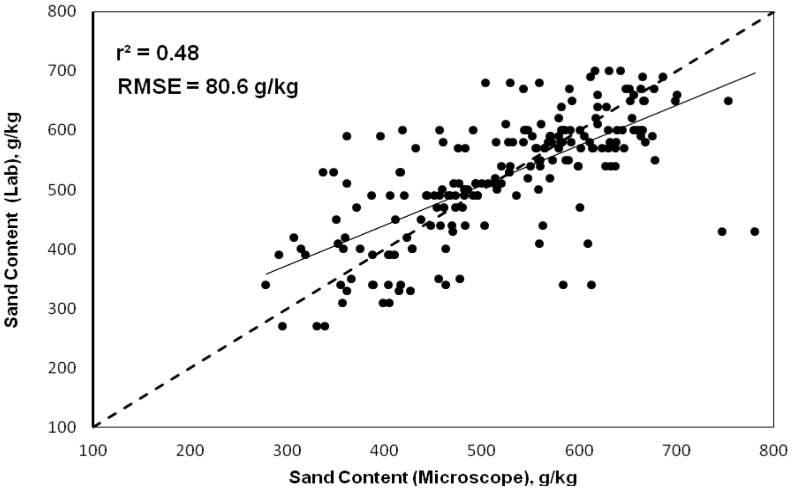

Fig. 4.7. Predicted particle sizes from images versus laboratory-measured particle sizes of coarse fraction for dataset 3.

4.2.3.1 Challenges in In-Situ Data Collection.

The sensor had several limitations when used *in-situ*. Soil moisture proved to be one of the major challenges. The image acquisition holder (described in section 3.1) was firmly pressed against the soil before the image was captured. This helped prevent the blurring in different regions of the image. However, the pressure on the soil caused soil moisture to ooze out of the soil matrix. This unintentionally created a slurry that made observing particles and definite edges in the soil difficult. Fig. 4.8(a) and 4.8(b) illustrate the difference between the microscopic images of moist soil and laboratory air dried soil. Images consisting of moist soil proved to be a challenge to the proposed algorithms.

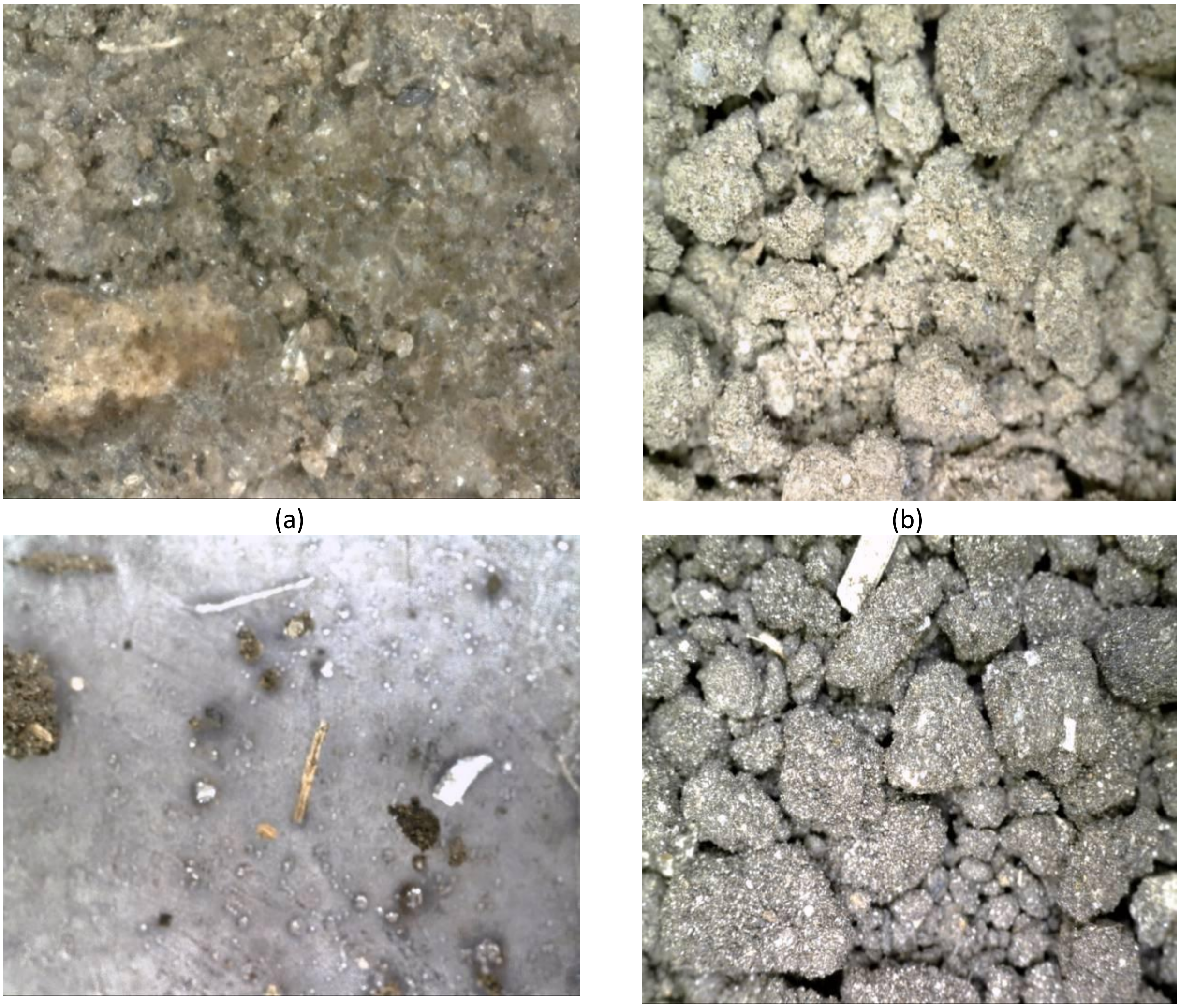

(a) (b)

(c) (d)

Fig.4.8. a) Field 86 Sample - 60 Replicate - 01 collected *in-situ* ; b) Field 86 Sample - 60 Replicate - 01 post air drying in laboratory. ; (c) F-26 Sample -22 Replicate -01 effect of LEDs on the sapphire window due to interaction with soil moisture ; d) Field 26 Sample - 22 Replicate - 01 post air drying in laboratory.

Non-uniform illumination and ambient light conditions pose a challenge to any computer vision algorithm. The microscope came equipped with a 7 LED ring used to illuminate the sample under observation. This was a useful feature as the holder was designed to block external light so that the sample was exposed to only the controlled uniform light of the 7 LEDs. However, the LEDs create significant amounts of heat and under cold conditions; heat the inner side of the fused silica window. During *in-situ* deployment, this heat produced a mist which formed on the outer side and the inner side of the lens due to high soil moisture. This proved to be problematic, slowing down field sampling and occasionally obscuring the entire image matrix. Fig. 4.8.(c) illustrates this particular problem. To address this problem, improvements in hardware design - specifically proper moisture insulation - could prevent misting of the lens. To resolve the issue LEDs were also on only during image acquisition for 5 ms per exposure.

Once these challenges are addressed the microscope image acquisition system could be suitable for stand-alone operation or use along with other sensors integrated on a multi-sensor platform for measuring sand and soil organic matter content directly in the field (Adamchuk et al., 2015).

5. SUMMARY AND CONCLUSIONS

This thesis presents the development of a microscope image acquisition system and a computer vision algorithm to estimate sand and organic matter content in soil. Study 1 reports on a spatial approach which resulted in the prediction of the sand content with RMSE of 84.7 g/kg and a color-based algorithm allowing the prediction of soil organic matter content with a RMSE of 0.11 log SOM using samples obtained from an agricultural field with an extremely high range of SOM (54.7-728 g/kg). This RMSE corresponds to 23.1 g/kg for mineral soil with 80 g/kg SOM and 231 g/kg for organic soil with 800 g/kg. Further testing is required on soils with diverse moisture conditions to test the reliability of the prediction algorithm.

Study 2 reports on the development of a wavelet transform algorithm for improved sand content estimation. While performing *ex-situ* measurements, the wavelet method predicted sand content with RMSE = 44.7 g/kg (organic soil) and RMSE = 40.2 g/kg (mineral soil). Both datasets did not require a calibration model, which indicates that this method actually measured particle size distribution and could result in superior accuracy when compared to the reference measurements (hydrometer). However, the *in-situ* measurements of mineral soil yielded RMSE = 80.6 g/kg. This increase was attributed to excess moisture present at the interface bertween the microscope holder and the soil being tested. A new holder design and lower soil moisture level at the time of measurement could reduce this effect.

Despite the superiority of the wavelet over the spatial image analysis in terms of sand content, the color-based prediction model appears to be the only valid technique that could be used to determine changes in soil organic matter content using the microscope imagery. The durable, low-cost portability of the microscope image acquisition system as well as the robustness of the algorithms make this sensor suitable for stand-alone operation or for use with other sensors integrated on a multi-sensor platform.

6 LIST OF REFERENCES

Adamchuk, V., N. Dhawale, B. Sudarsan, J. Kaur, and A. Biswas. 2015. Automated on-the-spot analysis of physical, chemical and biological soil properties. In: *Proceedings of the 4th Global Workshop on Proximal Soil Sensing*, Hangzhou, China, 12-15 May 2015, ed. Z. Shi, 1-8. Hangzhou, China: Zhejiang University.

Anton, A., Fekete, G., Darvas, B., & Székács, A. (2014). Environmental risk of chemical agriculture. *Engineering Tools for Environmental Risk Management: 1. Environmental Deterioration and Contamination-Problems and their Management, 1*, 93.

Barrios, E., & Trejo, M. (2002)., Special Issue on Ethnopedology (in press) Implications of local soil knowledge for integrated soil fertility management in Latin America. Geoderma, 67, *TSBF Institute.*

Bear, J. (2013). *Dynamics of fluids in porous media*: Courier Corporation, Mineola, New York.

Bezdicek, D. F., Papendick, R. I., & Lal, R. (1996). Introduction: Importance of soil quality to health and sustainable land management. *Methods of assessing soil quality. SSSA Spec. Publ, 49*, 1-18.

Biswas, A., Si, B., & Walley, F. (2008). Spatial relationship between δ 15 N and elevation in agricultural landscapes. *Nonlinear Processes in Geophysics, 15*(3), 397-407.

Biswas, A., & Si, B. C. (2011). Application of continuous wavelet transform in examining soil spatial variation: a review. *Mathematical Geosciences, 43*(3), 379-396.

Blackmer, A., & White, S. (1998). Blue arrow e-Alerts. *Australian Journal of Agricultural Research, 49*(3), 555-564.

Butler, J. B., Lane, S. N., & Chandler, J. H. (2001). Automated extraction of grain-size data from gravel surfaces using digital image processing. *Journal of Hydraulic Research, 39*(5), 519-529.

Chlaib, H. K., Mahdi, H., Al-Shukri, H., Su, M. M., Catakli, A., & Abd, N. (2014). Using ground penetrating radar in levee assessment to detect small scale animal burrows. *Journal of Applied Geophysics, 103*, 121-131.

Chui, C. K. (1992). Wavelets: a tutorial in theory and applications. *Wavelet Analysis and its Applications, San Diego, CA: Academic Press,| c1992, edited by Chui, Charles K., 1*.

Crida, R., & De Jager, G. (1997). An approach to rock size measurement based on a model of the human visual system. *Minerals engineering, 10*(10), 1085-1093.

Ford, A., & Roberts, A. (1998). Colour space conversions. *Westminster University, London, 1998*, 1-31.

Forsyth, D. A., & Ponce, J. (2002). *Computer Vision: A Modern Approach*: Prentice Hall Professional Technical Reference.

Francus, P. (1998). An image-analysis technique to measure grain-size variation in thin sections of soft clastic sediments. *Sedimentary Geology, 121*(3–4), 289-298. *doi:http://dx.doi.org/10.1016/S0037-0738(98)00078-5*

Gee, G. W., Bauder, J. W., & Klute, A. (1986). Particle-size analysis. *Methods of soil analysis. Part 1. Physical and mineralogical methods*, 383-411.

Ghalib, A. M., & Hryciw, R. D. (1999). Soil particle size distribution by mosaic imaging and watershed analysis. *Journal of Computing in Civil Engineering, 13*(2), 80-87.

Gökceoglu, C., & Aksoy, H. (1996). Landslide susceptibility mapping of the slopes in the residual soils of the Mengen region (Turkey) by deterministic stability analyses and image processing techniques. *Engineering Geology, 44*(1), 147-161.

Gómez-Robledo, L., López-Ruiz, N., Melgosa, M., Palma, A. J., Capitán-Vallvey, L. F., & Sánchez-Marañón, M. (2013). Using the mobile phone as Munsell soil-colour sensor: An experiment under controlled illumination conditions. *Computers and Electronics in Agriculture, 99*, 200-208. *doi:http://dx.doi.org/10.1016/j.compag.2013.10.002*

Gomez, C., Rossel, R. A. V., & McBratney, A. B. (2008). Soil organic carbon prediction by hyperspectral remote sensing and field vis-NIR spectroscopy: An Australian case study. *Geoderma, 146*(3), 403-411.

Gonzalez, R. C., Woods, R. E., & Eddins, S. L. (2004). *Digital image processing using MATLAB*: Pearson Education India, Noida, New Delhi.

Graps, A. (1995). An introduction to wavelets. *Computational Science & Engineering, IEEE, 2*(2), 50-61.

Haralick, R. M., & Shapiro, L. G. (1992). *Computer and Robot Vision*: Addison-Wesley Longman Publishing Co., Inc., Boston, Massachusetts.

Haralick, R. M., Sternberg, S. R., & Zhuang, X. (1987). Image analysis using mathematical morphology. *Pattern Analysis and Machine Intelligence, IEEE Transactions on, PAMI-9*(4), 532-550. *doi:10.1109/TPAMI.1987.4767941*

Hoogsteen, M., Lantinga, E., Bakker, E., Groot, J., & Tittonell, P. (2015). Estimating soil organic carbon through loss on ignition: effects of ignition conditions and structural water loss. *European Journal of Soil Science, 66*(2), 320-328.

Hryciw, R., & Raschke, S. (1996). Development of computer vision technique for in situ soil characterization. *Transportation Research Record: Journal of the Transportation Research Board,* 1526, 86-97.

Hryciw, R. D., Shin, S., & Jung, Y. (2006). Soil image processing: Single grains to particle assemblies. *CD Proceedings of Geotechnical Engineering In the Information Technology Age, ASCE GeoInstitute GeoCongress, Atlanta, GA.*

Hummel, J., Sudduth, K., & Hollinger, S. (2001). Soil moisture and organic matter prediction of surface and subsurface soils using an NIR soil sensor. *Computers and Electronics in Agriculture, 32*(2), 149-165.

Shonk, J. L., Gaultney, L. D., Schulze, D. G. & Scoyoc, G. E. V. (1991). Spectroscopic sensing of soil organic matter content. *Transactions of the ASAE, 34* (5), 1978-1984. .

Jackson, G. A., Logan, B. E., Alldredge, A. L., & Dam, H. G. (1995). Combining particle size spectra from a mesocosm experiment measured using photographic and aperture impedance (Coulter and Elzone) techniques. *Deep Sea Research Part II: Topical Studies in Oceanography, 42*(1), 139-157.

Jahedsaravani, A., Marhaban, M., Massinaei, M., Saripan, M., Mehrshad, N., & Noor, S. (2014). Development of a new algorithm for segmentation of flotation froth images. *Minerals & Metallurgical Processing Journal, 31*(1), 66-72.

Keener, J. D., Chalut, K. J., Pyhtila, J. W., Wax, A., Luo, B., He, S.,Pifferi, A. (2007). Application of Mie theory to determine the structure of spheroidal scatterers in biological materials. *Optics Letters, 32*(10), 1326-1328.

Krishnan, P., Alexander, J. D., Butler, B., & Hummel, J. W. (1980). Reflectance technique for predicting soil organic matter. *Soil Science Society of America Journal, 44*(6), 1282-1285.

Kumar, P., & Foufoula-Georgiou, E. (1997). Wavelet analysis for geophysical applications. *Reviews of Geophysics, 35*(4), 385-412.

Lau, K., & Weng, H. (1995). Climate signal detection using wavelet transform: How to make a time series sing. *Bulletin of the American Meteorological Society, 76*(12), 2391-2402.

Liu, Y. G., Liang, X. S., & Weisberg, R. H. (2007). Rectification of the bias in the wavelet power spectrum. *Journal of Atmospheric and Oceanic Technology, 24*(12), 2093-2102.

doi:10.1175/2007jtecho511.1

Mahboubi, A., Lal, R., & Faussey, N. (1993). Twenty-eight years of tillage effects on two soils in Ohio. *Soil Science Society of America Journal, 57*(2), 506-512.

Mallet, S. p. G. (1998). A Wavelet Tour of Signal Processing, 1998: Academic Press.

Mardia, K. V., Baczkowski, A., Feng, X., & Hainsworth, T. (1997). Statistical methods for automatic interpretation of digitally scanned finger prints. *Pattern Recognition Letters, 18*(11), 1197-1203.

Maurer Jr, C. R., Qi, R., & Raghavan, V. (2003). A linear time algorithm for computing exact Euclidean distance transforms of binary images in arbitrary dimensions. *Pattern Analysis and Machine Intelligence, IEEE Transactions on, 25*(2), 265-270.

Mertens, G., & Elsen, J. (2006). Use of computer assisted image analysis for the determination of the grain-size distribution of sands used in mortars. *Cement and Concrete Research, 36*(8), 1453-1459.

Meyer, F. (1994). Topographic distance and watershed lines. *Signal processing, 38*(1), 113-125.

Moga, A. N., & Gabbouj, M. (1998). Parallel Marker-Based Image Segmentation with Watershed Transformation. *Journal of Parallel and Distributed Computing, 51*(1), 27-45. *doi:10.1006/jpdc.1998.1448*

Mouazen, A., Maleki, M., De Baerdemaeker, J., & Ramon, H. (2007). On-line measurement of some selected soil properties using a VIS–NIR sensor. *Soil and Tillage Research, 93*(1), 13-27.

Nelson, D., & Sommers, L. E. (1982). Total carbon, organic carbon, and organic matter. *Methods of soil analysis. Part 2. Chemical and microbiological properties*(methodsofsoilan2), 539-579.

Noori, R., Karbassi, A., & Sabahi, M. S. (2010). Evaluation of PCA and Gamma test techniques on ANN operation for weekly solid waste prediction. *Journal of Environmental Management, 91*(3), 767-771.

Nordstrom, K. F., & Hotta, S. (2004). Wind erosion from cropland in the USA: a review of problems, solutions and prospects. *Geoderma, 121*(3), 157-167.

Otsu, N. (1975). A threshold selection method from gray-level histograms. *Automatica, 11*(285-296), 23-27.

Partal, T., & Küçük, M. (2006). Long-term trend analysis using discrete wavelet components of annual precipitations measurements in Marmara region (Turkey). *Physics and Chemistry of the Earth, Parts A/B/C, 31*(18), 1189-1200.

Percival, D. B., & Walden, A. T. (2006). *Wavelet methods for time series analysis* (Vol. 4): Cambridge University Press.

Pham, D. L., Xu, C., & Prince, J. L. (2000). Current methods in medical image segmentation 1. *Annual review of biomedical engineering, 2*(1), 315-337.

Roberts, D. F., Ferguson, R. B., Kitchen, N. R., Adamchuk, V. I., & Shanahan, J. F. (2012). Relationships between soil-based management zones and canopy sensing for corn nitrogen management. *Agronomy Journal, 104*(1), 119-129.

Robinson, W. (1927). The determination of organic matter in soils by means of hydrogen peroxide. *J. agric. Res, 34*, 339-356.

Scharf, P., Schmidt, J., Kitchen, N., Sudduth, K., Hong, S., Lory, J., & Davis, J. (2002). Remote sensing for nitrogen management. *Journal of Soil and Water Conservation, 57*(6), 518-524.

Schepers, A. R., Shanahan, J. F., Liebig, M. A., Schepers, J. S., Johnson, S. H., & Luchiari, A. (2004). Appropriateness of management zones for characterizing spatial variability of soil properties and irrigated corn yields across years. *Agronomy Journal, 96*(1), 195-203.

Schulze, D. G., Nagel, J. L., Van Scoyoc, G. E., Henderson, T. L., Baumgardner, M. F., & Stott, D. (1993). Significance of organic matter in determining soil colors. *Soil color*(soilcolor), 71-90.

Si, B. C. (2008). Spatial scaling analyses of soil physical properties: A review of spectral and wavelet methods. *Vadose Zone Journal, 7*(2), 547-562.

Smith, K. A., & Mullins, C. E. (1991). *Soil analysis: physical methods*: Marcel Dekker, Inc.

Sofou, A., Evangelopoulos, G., & Maragos, P. (2005). Soil image segmentation and texture analysis: a computer vision approach. *Geoscience and Remote Sensing Letters, IEEE, 2*(4), 394-398.

Soille, P. (1999). Morphological image processing: principles and applications: Cambridge University Press.

Stein, R. (1985). Rapid Grain-size Analyses of Clay and Silt Fraction by Sedigraph 5000d: Comparison with Coulter Counter and Atterberg Methods: RESEARCH METHOD PAPER. *Journal of Sedimentary Research, 55*(4).

Steinhardt, G. C., & Franzmeier, D. P. (1979). Comparison of organic matter content with soil color for silt loam soils of Indiana. *Communications in Soil Science and Plant Analysis, 10*(10), 1271-1277. *doi:10.1080/00103627909366981*

Taubner, H., Roth, B., & Tippkötter, R. (2009). Determination of soil texture: Comparison of the sedimentation method and the laser-diffraction analysis. *Journal of Plant Nutrition and Soil Science, 172*(2), 161-171.

Torrence, C., & Compo, G. P. (1998). A practical guide to wavelet analysis. *Bulletin of the American Meteorological Society, 79*(1), 61-78.

Tuceryan, M., & Jain, A. K. (1998). Texture analysis. *The handbook of pattern recognition and computer vision, 2*, 207-248.

Wang, X., Wang, T., Dong, Z., Liu, X., & Qian, G. (2006). Nebkha development and its significance to wind erosion and land degradation in semi-arid northern China. *Journal of Arid Environments, 65*(1), 129-141.

Weiss, B. (2006). Fast median and bilateral filtering. *ACM Trans. Graph., 25*(3), 519-526. *doi:10.1145/1141911.1141918*

White, D., Randolph, M., & Thompson, B. (2005). An image-based deformation measurement system for the geotechnical centrifuge. *International Journal of Physical Modelling in Geotechnics, 5*(3), 1-12.

Wilde, K., Rucka, M., & Tejchman, J. (2008). Silo music—Mechanism of dynamic flow and structure interaction. *Powder Technology, 186*(2), 113-129.

Yousefi, G., Safadoust, A., Mahboubi, A., Gharabaghi, B., Mosaddeghi, M., Ahrens, B., & Shirani, H. (2014). Bromide and lithium transport in soils under long-term cultivation of alfalfa and wheat. *Agriculture, Ecosystems & Environment, 188*, 221-228.

Strom, K., Kuhns, R., & Lucas, H. (2010). Comparison of automated image-based grain sizing to standard pebble-count methods. *Journal of Hydraulic Engineering, 136*(8), 461-473.

7 APPENDIX

A MATLAB Scripts for the Experiments

A.1 MATLAB Script For Spatial Analysis

```
        %% This script is designed to segment the foreground of the soil particles from the void space. This is followed by the Spatial moving window computations.

clc;
close all;
clear all;

imgDir = 'C:\soil project\algortihm tests\2015\F26_micro';
imgPath = strcat(imgDir, '/', '*.jpg'); % only take .jpg
imgFiles = dir(imgPath);
numImages = length(imgFiles);
 for img = 1:numImages
        I = imread(strcat(imgDir,'/', imgFiles(img).name));
        G2 = rgb2gray(I);
        [pathstr,f_name,ext] = fileparts(strcat(imgDir,'/',     imgFiles(img).name));
        Name(img,:)=cellstr(char(f_name));

        %% Porosity Calculation
        [rows columns numberOfColorChannels] = size(I);
        TotalArea = rows*columns;
```

```
g=rgb2gray(I);

g = histeq(g);

H=im2bw(g,0.65);


%% Pore data analysis

CC = bwconncomp(H);

CC2 = regionprops(CC,'area');

TotalPoreArea = bwarea(~H);

SoilArea = bwarea(H);

NumOfPores = CC.NumObjects ;

Diameter = (regionprops(CC,'EquivDiameter'));

A = {CC2};

Area = cell2mat(A);


c = {Diameter};

Diameter = cell2mat(c);


VoidRatio(img) = TotalPoreArea/SoilArea;

Porosity(img) = TotalPoreArea/TotalArea;

s(img).AreaOfEachPore = [CC2.Area]*4.1616;

s(img).Centroids = (regionprops(CC,'Centroid'))';

s(img).PoreDiameter = [Diameter.EquivDiameter]*2.04;

min_area(img)=min(s(img).AreaOfEachPore);

max_area(img)=max(s(img).AreaOfEachPore);
```

```
%% Image Masking window


ws=950;

C=0;

IM=mat2gray(G2);

mIM=imfilter(IM,fspecial('average',ws),'replicate');

sIM=mIM-IM-C;

bw=im2bw(sIM,0);

bw=imcomplement(bw);


ws2=380;

mIM2=imfilter(IM,fspecial('average',ws2),'replicate');

sIM2=mIM2-IM-C;

bw2=im2bw(sIM2,0);

bw2=imcomplement(bw2);

mIM3=min(mIM,mIM2);

sIM3=mIM3-IM-C;

bw3=im2bw(sIM3,0);

bw3=imcomplement(bw3);


filled = imfill(bw3, 'holes');

bw3=filled;

D = -bwdist(~bw3);
```

```
mask = imextendedmin(D,2);

D2 = imimposemin(D,mask);

Ld2 = watershed(D2);

bw3(Ld2 == 0) = 0;


b41=bwareaopen(bw3,400);

se = strel('square',10);

bw4=imerode(b41,se);

%% 2 Micro meters - Clay


A=G2;

mean=mean2(A);

std=std2(A);

B2=double(A-mean);

Standard_1=B2/std;


d = 1;

n = (d*2)+1;

m = (n+1)/2;

k = 0;

for i = [1:d:n]

            for j = [1:d:n]

                    k=k+1;

                    a(k,1) = i;
```

```
                    a(k,2) = j;
            end
end

ker = cell(1,9);
i = 0;
 for ii=1:9
            ker{ii} = zeros(n);
            ker{ii}(m,m) = 1;%// for center element
            i=i+1;
            ker{ii}(a(i,1),a(i,2)) = -1;
end

 interim = zeros( [size(Standard_1,1) size(Standard_1,2), numel(ker)] ); % allocate room
for intermediate results
 for ii=1:numel(ker)
            interim(:,:,ii) = conv2(Standard_1, ker{ii}, 'same' ); %//'same' takes care of
           output size
 end

interim =0.5*(interim.^2);
B = sum(interim,3);
B(B == 0) = NaN;
PC_full(img)=nanmean(nanmean(B));
```

```
A2=imresize(G2,[1900,1900]);

A2(~bw4) = 0;


A1=A2;


mean=mean2(A1);

std=std2(A1);

B1=double(A1-mean);

Standard=B1/std;


d = 1;

n = (d*2)+1;

m = (n+1)/2;

k = 0;

for i = [1:d:n]

        for j = [1:d:n]

                k=k+1;

                a(k,1) = i;

                a(k,2) = j;

                %c=horzcat(a,b)

        end

end


ker = cell(1,9);
```

```
i = 0;
 for ii=1:9
        ker{ii} = zeros(n);
        ker{ii}(m,m) = 1;%// for center element
        i=i+1;
        ker{ii}(a(i,1),a(i,2)) = -1;
 end

 interim = zeros( [size(Standard,1) size(Standard,2), numel(ker)] ); % allocates room for intermediate results
 for ii=1:numel(ker)
         interim(:,:,ii) = conv2(Standard, ker{ii}, 'same' ); %//'same' takes care of output size for you
 end

interim =0.5*(interim.^2);
B = sum(interim,3);
B(B == 0) = NaN;
PC_eroded(img)=nanmean(nanmean(B));

%% 10 Micrometer calculations

d1 = 5;
n1 = (d1*2)+1;
```

```
m1 = (n1+1)/2;
k1 = 0;
for i = [1:d1:n1]
        for j = [1:d1:n1]
                k1=k1+1;
                a1(k1,1) = i;
                a1(k1,2) = j;
        end
end

ker1 = cell(1,9);
i = 0;
 for ii=1:9
        ker1{ii} = zeros(n1);
        ker1{ii}(m1,m1) = 1;%// for center element
        i=i+1;
        ker1{ii}(a1(i,1),a1(i,2)) = -1;
 end

interim1 = zeros( [size(Standard_1,1) size(Standard_1,2), numel(ker1)] ); % allocate room for intermediate results
for ii=1:numel(ker1)
         interim1(:,:,ii) = conv2(Standard_1, ker1{ii}, 'same' ); %//'same' takes care of output size
```

```
 end


interim1 =0.5*(interim1.^2);

B = sum(interim1,3);

B(B == 0) = NaN;

PC_full_1(img)=nanmean(nanmean(B));


A2_1=imresize(G2,[1900,1900]);

A2_1(~bw4) = 0;


A1_1=A2_1;


mean1=mean2(A1_1);

std1=std2(A1_1);

B1=double(A1_1-mean1);

Standard1=B1/std1;


d1 = 5;

n1 = (d1*2)+1;

m1 = (n1+1)/2;

k1 = 0;

for i = [1:d1:n1]

        for j = [1:d1:n1]

                k1=k1+1;
```

```
                    a1(k1,1) = i;

                    a1(k1,2) = j;

            end

end


ker1 = cell(1,9);

i = 0;

 for ii=1:9

            ker1{ii} = zeros(n1);

            ker1{ii}(m1,m1) = 1;%// for center element

            i=i+1;

            ker1{ii}(a1(i,1),a1(i,2)) = -1;

end


for ii=1:numel(ker1)

             interim1(:,:,ii) = conv2(Standard, ker1{ii}, 'same' ); %//'same' takes care of
            output size for you

end


interim1 =0.5*(interim1.^2);

B = sum(interim1,3);

B(B == 0) = NaN;

PC_eroded_1(img)=nanmean(nanmean(B));

%% 50 Micrometer calculations
```

```
d2 = 10;
n2 = (d2*2)+1;
m2 = (n2+1)/2;
k2 = 0;

for i = [1:d2:n2]
        for j = [1:d2:n2]
                k2=k2+1;
                a2(k2,1) = i;
                a2(k2,2) = j;
        end
end

ker2 = cell(1,9);
i = 0;
 for ii=1:9
        ker2{ii} = zeros(n2);
        ker2{ii}(m2,m2) = 1;%// for center element
        i=i+1;
        ker2{ii}(a2(i,1),a2(i,2)) = -1;
end
```

```
 interim2 = zeros( [size(Standard_1,1) size(Standard_1,2), numel(ker2)] ); % allocate
room for intermidiate results
for ii=1:numel(ker2)
            interim2(:,:,ii) = conv2(Standard_1, ker2{ii}, 'same' ); %//'same' takes care of
            output size for you
 end


interim2 =0.5*(interim2.^2);
B = sum(interim2,3);
B(B == 0) = NaN;
PC_full_2(img)=nanmean(nanmean(B));


A2_2=imresize(G2,[1900,1900]);
A2_2(~bw4) = 0;
A1_2=A2_2;


mean2=mean2(A1_2);
std2=std2(A1_2);
B2=double(A1_2-mean2);
Standard1=B2/std2;


d2 = 10;
n2 = (d2*2)+1;
m2 = (n2+1)/2;
```

```
k2 = 0;
for i = [1:d2:n2]
        for j = [1:d2:n2]
                k2=k2+1;
                a2(k2,1) = i;
                a2(k2,2) = j;
         end
end

ker2 = cell(1,9);
i = 0;
 for ii=1:9
         ker2{ii} = zeros(n2);
         ker2{ii}(m2,m2) = 1;%// for center element
         i=i+1;
         ker2{ii}(a2(i,1),a2(i,2)) = -1;
 end

 interim2 = zeros( [size(Standard,1) size(Standard,2), numel(ker2)] ); % allocate room for
intermidiate results
 for ii=1:numel(ker2)
        interim2(:,:,ii) = conv2(Standard, ker2{ii}, 'same' ); %//'same' takes care of output
        size for you
 end
```

```
            interim2 =0.5*(interim2.^2);

            B = sum(interim2,3);

            B(B == 0) = NaN;

            PC_eroded_2(img)=nanmean(nanmean(B));


end

 %% output data formatting and computation

min_area=min_area';

max_area=max_area';

mean_area=mean_area';

std_area=std_area';

total_area=total_area';

VoidRatio=VoidRatio';

Porosity=Porosity';

save('s.mat');
```

A.2 MATLAB Script For Wavelet Analysis

```
%% This script is designed to apply global wavelet power spectrum (GWPS)on an image matrix the to estimate the coarse and fine soil fractions in data matrix.
clc;
close all;
clear all;
 %% Data Input
imgDir ='C:\Users\abiswa9\Desktop\Documents\Students\MSc Student supervised\Bharat\Bharath_image_database\2014_lab_images\R2';

J=imread('F86S27R3.bmp');
J = imresize(J,[960 1280]);
J=double(rgb2gray(J));
[imgWidth imgLength] = size(J);
xa=150;

%% Creating the sub-sampeld matrix
iL=48;
iB=64;
X=J(1:iL:end,:)';
[newrow newcol]=size(X);
numRows=20;
numScale=89;
sR(numRows).wave = zeros(numScale,numRows);
```

```
Y=J(:,1:iB:end);

numCols=20;

numScale=89;

sC(numCols).wave = zeros(numScale,numCols);


 %% For selected rows

for i = 1:numRows

            sst=X(:,i);

            [d,dt]=formatts(sst);

            n=size(d,1);

            sigma2=var((d(:,2)));

            Args=struct('Pad',1,... % pad the time series with zeroes (recommended)

            'Dj',1/12, ... % this will do 12 sub-octaves per octave

            'S0',2*dt,... % this says start at a scale of 2 years

            'J1',[],...

            'Mother','Morlet', ...

            'MaxScale',[],... %a more simple way to specify J

            MakeFigure',(nargout==0),...

            'BlackandWhite',0,...

            'AR1','auto');

            if isempty(Args.J1)

                        if isempty(Args.MaxScale)

                                    Args.MaxScale=(n*.17)*2*dt; %automaxscale
```

```
    end
    Args.J1=round(log2(Args.MaxScale/Args.S0)/Args.Dj);
end

if strcmpi(Args.AR1,'auto')
    Args.AR1=ar1nv(d(:,2));
    if any(isnan(Args.AR1))
        error('Automatic AR1 estimation failed. Specify it manually (use arcov or
        arburg).')
    end
end

% Wavelet transofrm
[wave,period,scale,coi] =
wavelet(d(:,2),dt,Args.Pad,Args.Dj,Args.S0,Args.J1,Args.Mother);
s(i).power =(abs(wave)).^2 ;  % compute wavelet power spectrum
signif(i,:) = wave_signif(1.0,dt,scale,0,Args.AR1,-1,-1,Args.Mother);
s(i).sig95 = (signif(i,:)')*(ones(1,n)); % expand signif --> (J+1)x(N) array
s(i).sig95 = s(i).power ./ (sigma2*s(i).sig95);
s(i).wave = wave;

% Global wavelet spectrum & significance levels:
s(i).global_ws = sigma2*(sum(s(i).power')/n); % time-average over all times
dof = n - scale; % the -scale corrects for padding at edges
```

```
s(i).global_signif = wave_signif(sigma2,dt,scale,1,Args.AR1,-1,dof,Args.Mother);


% rectification of bias

for j=1:length(scale)

        s(i).power_mod(j,:) = s(i).power(j,:)/scale(j);

end

s(i).global_ws_mod = sigma2*(sum(s(i).power_mod')/n); % time-average over all times

dof = n - scale; % the -scale corrects for padding at edges

s(i).global_signif_mod = wave_signif(sigma2,dt,scale,1,Args.AR1,-1,dof,Args.Mother);


period_mat(i,:)= period;

scale_mat(i,:)= scale;

coi_mat(i,:)= coi;


x=scale;

% xa = 180; % partial value point in scale (50 microns/ 2.10 microns per pixel = 23.8)

xb = max(x);


y=s(i).global_ws_mod;

ind = (x > xa) & (x < xb);

xw = x(ind);

yw = y(ind);


ya_r = interp1(x, y, xa, 'spline');
```

```
        yb_r = interp1(x, y, xb, 'spline');
        xw = [xa, xw, xb];
        yw = [ya_r, yw, yb_r];

        h1 = spline(x,y);
        coeffs = h1.coefs;
        Full_area=trapz(x,y);
        interim = trapz(xw, yw);
        Partial_area=Full_area-interim;
        s(i).silt_clay=(Partial_area/Full_area)*100;
        s(i).sand=100-s(i).silt_clay;
        Fine_R(i)=s(i).silt_clay;
        Coarse_R(i)=s(i).sand;
end

%% For selected columns
for p = 1:numCols
        sst=Y(:,p);
        [d,dt]=formatts(sst);
        n=size(d,1);
        sigma2=var((d(:,2)));
        %d(:,2) = (d(:,2) - mean(d(:,2)))/ std(d(:,2));
        Args=struct('Pad',1,... % pad the time series with zeroes (recommended)
        'Dj',1/12, ... % this will do 12 sub-octaves per octave
```

```
'S0',2*dt,... % this says start at a scale of 2 years

'J1',[],...

'Mother','Morlet', ...

'MaxScale',[],... %a more simple way to specify J

'MakeFigure',(nargout==0),...

'BlackandWhite',0,...

'AR1','auto');

if isempty(Args.J1)

            if isempty(Args.MaxScale)

                        Args.MaxScale=(n*.17)*2*dt; %automaxscale

             end

            Args.J1=round(log2(Args.MaxScale/Args.S0)/Args.Dj);

end


if strcmpi(Args.AR1,'auto')

Args.AR1=ar1nv(d(:,2));

            if any(isnan(Args.AR1))

                        error('Automatic AR1 estimation failed. Specify it manually (use arcov or

                                    arburg).')

            end

end

% Wavelet transform

[wave1,period1,scale1,coi1] =

wavelet(d(:,2),dt,Args.Pad,Args.Dj,Args.S0,Args.J1,Args.Mother);
```

```
s(p).power1 =(abs(wave1)).^2 ;  % compute wavelet power spectrum
signif1(p,:) = wave_signif(1.0,dt,scale1,0,Args.AR1,-1,-1,Args.Mother);
s(p).sig951 = (signif1(p,:)')*(ones(1,n)); % expand signif --> (J+1)x(N) array
s(p).sig951 = s(p).power1 ./ (sigma2*s(p).sig951);
s(p).wave1 = wave1;

% Global wavelet spectrum & significance levels:
s(p).global_ws1 = sigma2*(sum(s(p).power1')/n); % time-average over all times
dof = n - scale1; % the -scale corrects for padding at edges
s(p).global_signif1 = wave_signif(sigma2,dt,scale1,1,Args.AR1,-1,dof,Args.Mother);

% rectification of bias
for j=1:length(scale1)
        s(p).power_mod1(j,:) = s(p).power1(j,:)/scale1(j);
end
s(p).global_ws_mod1 = sigma2*(sum(s(p).power_mod1')/n); % time-average over all times
dof = n - scale1; % the -scale corrects for padding at edges
s(p).global_signif_mod1 = wave_signif(sigma2,dt,scale1,1,Args.AR1,-1,dof,Args.Mother);

period_mat_c(p,:)= period1;
scale_mat_c(p,:)= scale1;
coi_mat_c(p,:)= coi1;
```

```
x=scale1;

% xa = 180; % partial value point in scale (50 microns/ 2.10 microns per pixel = 23.8)

xb = max(x);


y=s(p).global_ws_mod1;

ind1 = (x > xa) & (x < xb);

xw = x(ind1);

yw = y(ind1);


ya_r = interp1(x, y, xa, 'spline');

yb_r = interp1(x, y, xb, 'spline');

xw = [xa, xw, xb];

yw = [ya_r, yw, yb_r];


h1 = spline(x,y);

coeffs = h1.coefs;

Full_area1=trapz(x,y);

interim1 = trapz(xw, yw);

Partial_area1=Full_area1-interim1;

s(p).silt_clay1=(Partial_area1/Full_area1)*100;

s(p).sand1=100-s(p).silt_clay1;

Fine_C(p)=s(p).silt_clay1;

Coarse_C(p)=s(p).sand1;
```

```
end


%% average of row and col prediction

Fine_Avg = (Fine_C+Fine_R)/2;

Fine_a=mean(Fine_Avg)

Coarse_Avg = (Coarse_C+Coarse_R)/2;

Coarse_a= mean(Coarse_Avg)
```

B Laboratory Datasets of Soil Samples

Table B.1 - Field 26 - Summer 2014 Dataset

Sample Id	Sand(g/kg)	Silt(g/kg)	Clay(g/kg)	OM(g/kg)
1	134	147	86	633
2	575	227	120	78
3	430	259	237	75
4	462	255	229	55
5	124	124	24	728
6	460	318	43	179
7	183	201	111	505
8	288	142	232	338
9	222	528	66	183
10	510	191	225	75
11	470	198	254	77
12	291	365	72	271
13	328	404	53	214
14	382	255	218	145
15	474	237	219	70
16	288	169	120	423
17	179	89	63	668
18	34	229	98	639
19	281	322	47	350
20	160	528	85	227
21	421	229	225	125
22	253	287	32	428
23	114	212	31	643
24	122	159	20	699
25	245	164	71	520
26	174	229	113	484
27	441	270	105	185
28	360	382	121	138
29	174	309	161	357
30	527	329	48	96
31	420	300	33	247
32	586	314	31	68
33	416	249	179	156
34	429	242	121	207
35	283	281	134	301
36	239	177	134	450
37	588	228	121	62

Table B.1(continued) - Field 26 - Summer 2014 Dataset

Sample Id	Sand(g/kg)	Silt(g/kg)	Clay(g/kg)	OM(g/kg)
38	593	169	173	65
39	539	284	33	144
40	476	380	44	100
41	494	121	191	194
42	465	159	198	178
43	483	298	34	185
44	80	387	29	505
45	182	201	107	510
46	302	394	39	265
47	211	207	118	464
48	370	293	95	243
49	319	426	41	213
50	272	372	29	327
51	219	155	93	534
52	186	65	192	557
53	183	118	375	324
54	275	181	244	301
55	288	148	316	248
56	374	257	219	150

Table B.2 - Field 86 - Summer 2015 Dataset

Sample ID	% Sand	% Silt	% Clay	Organic Matter LOI%
1	34	35	31	7.0
2	60	19	21	6.2
3	31	22	47	9.4
4	65	26	9	6.2
6	43	24	33	6.1
5	66	21	13	4.2
7	65	24	11	5.0
8	54	29	17	6.4
9	57	24	19	5.2
10	40	23	37	6.2
11	57	24	19	4.9
12	34	35	31	6.6
13	53	26	21	4.7
14	59	26	15	5.1
15	60	21	19	3.3
16	58	25	17	4.5
17	52	29	19	5.9
18	68	21	11	3.9
19	60	23	17	5.4
20	70	17	13	3.7
21	60	23	17	4.9
22	58	25	17	4.7
23	57	24	19	5.5
24	49	26	25	6.9
25	57	26	17	5.9
26	62	21	17	6.0
27	41	30	29	6.9
28	47	30	23	5.3
29	55	24	21	5.1
30	39	26	35	6.1
31	50	22	28	4.3
32	57	19	24	4.9
33	49	21	30	5.0
34	61	18	21	4.7
35	69	19	12	4.6
36	51	28	21	5.4
37	45	28	27	6.5
38	59	23	18	5.3

Table B.2 (continued) - Field 86 - Summer 2015 Dataset

Sample ID	% Sand	% Silt	% Clay	Organic Matter LOI%
39	50	26	24	6.2
40	58	25	17	4.4
41	44	21	35	5.7
42	40	30	30	6.9
43	60	26	14	6.2
44	60	25	15	5.1
45	42	43	15	9.8
46	64	19	17	6.3
47	67	16	17	6.7
48	49	16	35	8.2
49	53	20	27	6.5
50	33	24	43	8.5
51	27	20	53	8.6
52	35	28	37	7.0
53	67	16	17	4.3
54	51	30	19	5.7
55	49	22	29	7.0
56	49	18	33	7.2
57	39	26	35	6.6
58	58	23	19	5.6
59	51	26	23	5.1
60	47	28	25	5.3
61	59	20	21	4.5
62	55	32	13	5.2
63	58	27	15	5.2
64	54	29	17	4.6
1A	34	35	31	7.0
2A	44	35	21	6.5
3A	54	15	31	5.6